Journal of Luminescence 298 (2026) 122050

Contents lists available at ScienceDirect

Journal of Luminescence

journal homepage: www.elsevier.com/locate/jlumin

Full Length Article

Structure–property correlation and tunable luminescence in Dy^{3+}-activated $YBa_3B_9O_{18}$ phosphors via alkali co-doping

O. Madkhali [a], Jabir Hakami [a], H. Aydin [b,c], Ş. Demiç [b,d], M. Can [e], U.H. Kaynar [f], M.B. Coban [g], N. Can [a,*]

[a] Jazan University, College of Science, Department of Physical Sciences, Physics Division, P.O. Box 114, Jazan, 45142, Saudi Arabia
[b] Graphene Application&Research Center, Izmir Katip Celebi University, Izmir, Turkiye
[c] Central Research Laboratories, Izmir Katip Celebi University, Izmir, Turkiye
[d] Faculty of Engineering and Architecture, Department of Metallurgical and Materials Engineering, Izmir Kâtip Celebi University, Izmir, Turkiye
[e] Department of Engineering Sciences, Izmir Katip Celebi University, Izmir, Turkiye
[f] Bakırcay University, Faculty of Engineering and Architecture, Department of Fundamental Sciences, Menemen, Izmir, Turkiye
[g] Balikesir University, Faculty of Arts and Sciences, Department of Physics, Balikesir, Turkiye

ARTICLE INFO

Keywords:
$YBa_3B_9O_{18}$
Dy^{3+} phosphor
Alkali co-doping
Judd–Ofelt
Luminescence
Thermal stability

ABSTRACT

Borate-based hosts are attractive candidates for phosphor-converted white light-emitting diodes (pc-WLEDs) owing to their wide band gaps, chemical stability, and structural flexibility. In this work, Dy^{3+}-activated $YBa_3B_9O_{18}$ (YBBO) phosphors co-doped with Na^+ and K^+ ions were synthesized to investigate the influence of alkali-induced structural modification on photoluminescence behavior. X-ray diffraction and Rietveld refinement confirmed the formation of a single-phase hexagonal structure, while crystallite-size and microstrain analyses indicated that K^+ co-doping introduces relatively higher lattice distortion than Na^+. Photoluminescence spectra under near-UV excitation exhibited characteristic Dy^{3+} emissions at ~576, 660, and 760 nm, corresponding to yellow, red, and deep-red transitions, respectively. The optimum Dy^{3+} concentration was found to be $x = 0.05$, beyond which concentration quenching occurs mainly through long-range multipolar interactions, as supported by the critical transfer distance of ~8.8 Å. Alkali co-doping enhanced the PL intensity, with Na^+ giving the highest enhancement (~1.8-fold), whereas K^+ increased the relative contribution of the 660 nm red emission band. Emission-derived Judd–Ofelt-type analysis indicated an increased $\Omega_{4,eff}$ trend, which is discussed only as a comparative indicator of the enhanced relative contribution of the 660 nm red band rather than as an absolute Judd–Ofelt parameter. Temperature-dependent PL analysis showed improved thermal stability for the co-doped samples, with activation energies of ~0.202 eV for Na^+ and ~0.189 eV for K^+. At 550 K, the co-doped phosphors retained approximately 40% of their room-temperature emission intensity, compared with ~23% for the singly doped sample. Chromaticity analysis placed the emission in the warm-white to yellow-red region, mainly governed by the relative contributions of the 576 nm yellow and 660 nm red bands. Overall, the results suggest an indirect structure–luminescence relationship in YBBO:Dy^{3+} phosphors and demonstrate that alkali co-doping is an effective strategy for tuning emission intensity, color output, and thermal stability.

1. Introduction

Phosphor-converted white light-emitting diodes (pc-WLEDs) have become key candidates to replace conventional lighting due to their high efficiency, long lifetime, and environmental friendliness. The performance of pc-WLEDs strongly depends on the properties of the down-conversion phosphors, which must combine high luminescence efficiency, good color quality (e.g., appropriate correlated color temperature (CCT) and color rendering index (CRI)), and excellent thermal stability under near-UV or blue excitation [1–5]. Rare-earth-doped inorganic hosts, especially borates, niobates and phosphates, are widely explored to meet these requirements [6–9].

Rare-earth (RE^{3+}) ions have attracted considerable attention as luminescent activators because of their rich 4f electronic configurations, which enable efficient and spectrally narrow emissions across the visible region. Depending on the activator ion, a wide range of emission colors

* Corresponding author.
E-mail address: ncan@jazanu.edu.sa (N. Can).

https://doi.org/10.1016/j.jlumin.2026.122050
Received 29 April 2026; Received in revised form 23 June 2026; Accepted 28 June 2026
Available online 29 June 2026

can be achieved, including blue emission from Tm^{3+}, green emission from Tb^{3+}, yellow emission from Dy^{3+}, orange-red emission from Sm^{3+}, and intense red emission from Eu^{3+}. Owing to these characteristics, rare-earth-doped phosphors have been extensively investigated for applications in phosphor-converted white light-emitting diodes (pc-WLEDs), display technologies, optical communication systems, solid-state lasers, and other photonic devices [10,11]. The luminescence performance of these materials strongly depends on the interaction between the activator ion and the host lattice, making the selection and engineering of suitable host structures an important research topic. Among rare-earth activators, Dy^{3+} is particularly attractive because its $^4F_{9/2} \rightarrow {}^6H_{15/2}$ (blue) and $^4F_{9/2} \rightarrow {}^6H_{13/2}$ (yellow) transitions can be combined to generate single-phase white or warm-white emission in diverse hosts [12–15]. Dy^{3+}-activated phosphors have been extensively investigated for solid-state lighting applications because the simultaneous blue and yellow emissions can produce near-white light under near-UV excitation. For example, Baig et al. reported that $Ca_2Pb_3(PO_4)_3Cl:Dy^{3+}$ exhibits intense blue (≈482 nm) and yellow (≈576 nm) emissions, high color purity, and well-defined concentration quenching behavior, highlighting the suitability of Dy^{3+} as a single-activator white-light emitter [16]. The $^4F_{9/2} \rightarrow {}^6H_{13/2}$ transition is hypersensitive and strongly influenced by local asymmetry, whereas the $^4F_{9/2} \rightarrow {}^6H_{15/2}$ transition is relatively insensitive and their intensity ratio serves as a sensitive probe of the crystal-field environment around Dy^{3+} [17–19]. In Dy^{3+}-activated borates and related oxides, this sensitivity links local symmetry and bonding to color coordinates, concentration quenching behavior, and Judd–Ofelt intensity parameters [17,20–25]. Conventional Judd–Ofelt (J–O) analysis provides quantitative insight into radiative transition probabilities and local asymmetry through the intensity parameters Ω_2, Ω_4, and Ω_6 obtained from absorption spectroscopy, which are highly sensitive to changes in the coordination environment of Dy^{3+} ions. In particular, alkali co-doping has been reported to modify these absorption-derived Judd–Ofelt parameters, reflecting changes in local asymmetry and covalency around Dy^{3+} and correlating with enhanced electric-dipole emission and reduced non-radiative losses [26,27]. In the present work, however, emission-derived effective intensity parameters ($\Omega_{2,\mathrm{eff}}$, $\Omega_{4,\mathrm{eff}}$, and $\Omega_{6,\mathrm{eff}}$) are employed as comparative indicators of crystal-field modification rather than absolute Judd–Ofelt parameters.

Borate-based hosts are of particular interest because of their wide band gaps, good chemical stability and flexible framework that can accommodate different cations, enabling fine tuning of the Dy^{3+} environment [7,28]. The $YBa_3B_9O_{18}$ host possesses a complex borate framework with multiple cationic sites (Y^{3+}, Ba^{2+}), offering distinct coordination environments that can modulate activator distribution, crystal-field symmetry, and luminescence properties. Considering charge balance and ionic radii, Dy^{3+} ions are expected to preferentially substitute Y^{3+} sites, while alkali ions (Li^+, Na^+, K^+) may occupy interstitial positions or substitute Ba^{2+}-related sites, leading to local charge imbalance and symmetry distortion. These structural modifications are expected to influence the crystal field strength and non-radiative relaxation pathways of Dy^{3+}. Furthermore, alkali ($Li^+/Na^+/K^+$) co-doping has emerged as an effective strategy to improve charge compensation, relax lattice strain and modify site symmetry, leading to enhanced photoluminescence and often improved thermal stability in Dy^{3+} or Eu^{3+} activated hosts [4,8,29,30]. For instance, Yadav et al. demonstrated that Li^+ co-doping in $MgTiO_3:Dy^{3+}$ significantly improves crystallinity and particle growth, resulting in an approximately three-fold enhancement of the characteristic Dy^{3+} yellow emission through charge-compensation and local structural modification mechanisms [31]. These findings indicate that alkali-ion co-doping is an effective approach for tailoring the local crystal-field environment and luminescence efficiency of Dy^{3+}-activated phosphors. Recent studies have further highlighted the importance of defect and site engineering in borate-based phosphors. For example, Dy^{3+}/Eu^{3+} co-doping in $Ba_2CaB_2Si_4O_{14}$ has been shown to enable tunable warm-white emission, improved thermal stability, and efficient energy-transfer processes [32]. In addition, Na^+ co-doping in $Ba_2CaB_2Si_4O_{14}$-based phosphors has been reported to act as an effective charge compensator and site-environment modifier, leading to optimized luminescence performance and color tunability [33]. These findings further demonstrate the important role of alkali ions and defect regulation in tailoring the optical properties of borate-related hosts and provide additional motivation for investigating Na^+ and K^+ co-doping effects in $YBa_3B_9O_{18}^{3+}$ phosphors. Motivated by these observations, differences in ionic radii ($Li^+ < Na^+ < K^+$) are expected to induce varying degrees of lattice distortion and crystal-field modification. These variations can influence the Dy^{3+} emission characteristics, including the blue–yellow intensity ratio, overall luminescence efficiency, and thermal quenching behavior [3,34]. While $Li^+/Na^+/K^+$ co-doping has been shown to enhance Dy^{3+} emission and thermal stability in vanadate and molybdate hosts via charge compensation and local distortion [4,26], an analogous quantitative comparison of alkali-ion co-doping effects within a single complex borate framework, coupled with Judd–Ofelt analysis and activation-energy evaluation, has not yet been systematically investigated. In particular, the relationship between alkali-induced lattice distortion, crystal-field modification, and emission-derived Judd–Ofelt parameters remains largely unexplored in $YBa_3B_9O_{18}$-based phosphors.

A key novelty of the present study is the use of alkali-ion co-doping as a controlled approach to systematically tailor the structural and optical properties of Dy^{3+}-activated $YBa_3B_9O_{18}$. Although alkali-assisted emission enhancement has been reported in several Dy^{3+}-activated phosphor systems, the specific relationship between alkali-induced structural distortion and Dy^{3+} luminescence behavior in the $YBa_3B_9O_{18}$ borate framework has not been systematically clarified. Unlike previous studies that mainly reported emission enhancement through alkali incorporation in different host lattices, the present work provides a direct comparison of Na^+ and K^+ co-doping within the same borate framework. This comparison enables the distinct roles of Na^+ and K^+ ions to be evaluated in terms of lattice parameters, crystallite size, microstrain, local structural disorder, emission intensity redistribution, lifetime behavior, and thermal quenching resistance. By combining crystallographic analysis, lattice strain evaluation, photoluminescence spectroscopy, thermal quenching measurements, lifetime analysis, and emission-derived Judd–Ofelt parameters, the present work establishes an integrated structure–property framework linking alkali-induced lattice modification with crystal-field variation and tunable Dy^{3+} emission. This approach offers new insight into the role of alkali co-doping in complex borate phosphors and provides guidance for the design of thermally stable Dy^{3+}-based phosphors for pc-WLED applications.

Thermal quenching, governed by non-radiative relaxation through phonon-assisted processes, is a critical limitation for high-power pc-WLEDs and can be quantitatively assessed via activation energy analysis of temperature-dependent PL [4,13], thereby enabling comparison of thermal robustness with other Dy^{3+}-activated borate and oxide phosphors where activation energies have been evaluated using similar approaches. This behavior can be further interpreted using the configurational coordinate model, where thermally activated crossover from excited states to non-radiative pathways competes with radiative emission.

In this context, this work addresses the lack of a systematic and comparative understanding of alkali-induced lattice distortion effects on the crystal-field environment and radiative properties of Dy^{3+} in complex borate hosts, particularly $YBa_3B_9O_{18}$. It is hypothesized that controlled Na^+/K^+ co-doping in $YBa_3B_9O_{18}:Dy^{3+}$ can modulate lattice strain, local symmetry, and non-radiative pathways, thereby enabling optimization of emission intensity, color balance, and thermal stability. Dy^{3+}-doped $YBa_3B_9O_{18}$ phosphors co-doped with Na^+, and K^+ are therefore synthesized and comprehensively characterized by X-ray diffraction (XRD) with Rietveld refinement for structural analysis, combined spectroscopic techniques (Raman, FTIR, and photoluminescence, including high-temperature PL), emission-derived

Judd–Ofelt-type analysis, lifetime measurements, and complementary morphological and chromaticity studies (SEM/EDS and CIE coordinates). By establishing an indirect and comparative correlation between XRD-derived structural distortion, emission-derived effective Judd–Ofelt parameters, and emission behavior, this work provides a coherent structure–property framework for tuning luminescence performance in Dy^{3+}-activated borate phosphors. It should be emphasized that the proposed structure–property relationship is based on average structural and spectroscopic evidence, and does not represent a direct determination of the local coordination environment around Dy^{3+} ions.

2. Experiments

2.1. Preparation of Dy^{3+}-Doped $YBa_3B_9O_{18}$ phosphors with alkali Co-doping

Dy^{3+}-activated $YBa_3B_9O_{18}$ (YBBO) phosphors co-doped with alkali ions (Na^+ and K^+) were successfully synthesized using a combustion-assisted route. All starting materials were of analytical grade and utilized as received without additional purification. The host matrix was constructed using yttrium oxide (Y_2O_3, 99.8%, Sigma-Aldrich), barium nitrate ($Ba(NO_3)_2$, 99.99%, Sigma-Aldrich), and boric acid (H_3BO_3), while Dy^{3+} ions were introduced through an appropriate precursor in accordance with the desired doping concentration. The alkali co-dopants (Na^+ and K^+) were incorporated in varying amounts ranging from 0.5 to 7 wt% to systematically investigate their influence on the material properties.

In the initial step, Y_2O_3 was converted into a nitrate form by dissolving it in dilute nitric acid under continuous magnetic stirring until a clear yttrium nitrate solution was obtained. The stoichiometric ratios of Y, Ba, B, Dy, and alkali ions were calculated based on the target composition. The precursors were then thoroughly mixed in an agate mortar with a small quantity of deionized water to ensure uniform dispersion and compositional consistency. To facilitate the combustion process and promote homogeneous mixing at the molecular scale, urea ($CO(NH_2)_2$) and glycine ($C_2H_5NO_2$) were introduced as fuel agents. The resulting solution was heated at 120 °C overnight to remove excess moisture and stabilize the precursor matrix. The dried material was subsequently subjected to a two-step thermal treatment. Initially, a pre-calcination process was carried out at 600 °C for 4 h in air to decompose organic constituents and remove volatile species. After intermediate grinding, the powders were further sintered at 950 °C for 6 h to achieve improved crystallinity and phase formation.

Following natural cooling to room temperature inside the furnace, the final phosphor powders were collected and stored in airtight containers to prevent moisture uptake. This synthesis approach enabled the controlled fabrication of Dy^{3+}-doped YBBO phosphors with Na^+/K^+ co-doping, providing high crystallinity and phase stability. Moreover, the adopted strategy allows systematic evaluation of the role of alkali ions and Dy^{3+} concentration on the luminescence and thermally stimulated properties of the host lattice.

The formation of Dy^{3+}-doped YBBO phosphors can be described by a simplified overall reaction as follows:

$$(1-x)Y_2O_3 + xDy_2O_3 + 3Ba(NO_3)_2 + 3H_3BO_3 \rightarrow 2Y_{1-x}Dy_xBa_3(BO_3)_3 + gaseous\ products$$

In the presence of alkali co-doping (Na^+/K^+), the composition can be expressed as:

$$Y_{1-x}Dy_x(Ba_3)_3 + yA^+ \rightarrow Y_{1-x-y}Dy_xA_yBa_3(BO_3)_3$$

where A^+ represents Na^+ or K^+ ions, and x and y correspond to the dopant concentrations.

It is important to note that the combustion synthesis involves complex redox reactions between metal nitrates and fuel agents (urea and glycine), resulting in the release of gaseous species such as CO_2, N_2, and H_2O. Therefore, the above equations represent the overall phase formation rather than a fully balanced reaction mechanism.

2.2. Characterization techniques

The crystallographic structure and phase purity of Dy^{3+}-activated $YBa_3B_9O_{18}$ phosphors co-doped with Na^+ or K^+ ions were examined using X-ray diffraction (XRD) analysis performed on a Malvern Panalytical Empyrean diffractometer equipped with Cu-Kα radiation ($\lambda = 1.5418$ Å), operating at 45 kV and 40 mA. Diffraction data were recorded at ambient conditions across a 2θ range of 10° to 80°. Structural parameters, including lattice constants and crystallite size, were subsequently determined via Rietveld refinement employing standard crystallographic analysis software. Microstructural features and elemental composition were evaluated through scanning electron microscopy (SEM, Zeiss) coupled with energy-dispersive X-ray spectroscopy (EDS). To mitigate surface charging and enhance conductivity, the samples were coated with a thin gold layer prior to SEM examination. The vibrational characteristics and local bonding environment of the host lattice were investigated using Fourier-transform infrared (FTIR) spectroscopy (Thermo Scientific Nicolet iS50) within the spectral range of 400–4000 cm^{-1}. Complementary Raman measurements were carried out using a Renishaw inVia Raman microscope equipped with a 532 nm excitation laser and a 2400 lines/mm grating, enabling detailed analysis of lattice dynamics and vibrational modes. Photoluminescence excitation (PLE) and emission (PL) spectra were obtained using an Edinburgh Instruments FS5 spectrofluorometer with a xenon lamp as the excitation source. Temperature-dependent optical measurements were conducted from room temperature up to 550 K to assess luminescence behavior under varying thermal conditions. The evolution of emission intensity and spectral characteristics with increasing temperature was analyzed to evaluate thermal stability and activation mechanisms relevant to potential device applications.

3. Results and discussions

3.1. Crystal structure and rietveld refinement analysis

Fig. 1a presents the X-ray diffraction (XRD) patterns of undoped YBBO alongside Dy^{3+}-doped and alkali co-doped compositions. All diffraction peaks are well indexed to the reference pattern (JCPDS card no. 98-017-0217), confirming the formation of a single-phase hexagonal structure with the space group $P6_3/m$, without detectable secondary phases. The preservation of peak positions and profiles upon Dy^{3+} incorporation indicates that the host lattice remains structurally stable, which is essential for suppressing defect-related emission centers in subsequent photoluminescence analysis. Minor variations in peak intensity and slight shifts in 2θ positions are observed after doping, which can be attributed to lattice distortion induced by ionic substitution. The observed peak shifts relative to the standard JCPDS pattern are associated with slight variations in lattice parameters and d-spacing caused by Dy^{3+} substitution and alkali-ion incorporation. The resulting local strain and crystal-lattice distortion are consistent with the refined structural parameters and microstrain values obtained from the Rietveld and Williamson–Hall analyses.

The crystal structure visualization (Fig. 1b) highlights the coordination environment within $YBa_3B_9O_{18}$, which consists of a complex borate framework containing B–O structural units, YO_6 octahedra, and Ba–O coordination polyhedral. The Y^{3+} ions occupy octahedral sites, making them the most probable substitution sites for Dy^{3+} ions. This is further supported by ionic radius considerations (Table 1). The calculated ionic radius mismatch (D_r) between Y^{3+} and Dy^{3+} is ~12.22%, well below the 30% threshold, confirming favorable substitution. This result is consistent with the identical coordination number (CN = 6) of Y^{3+} and Dy^{3+} ions, further supporting the preferential substitution at the

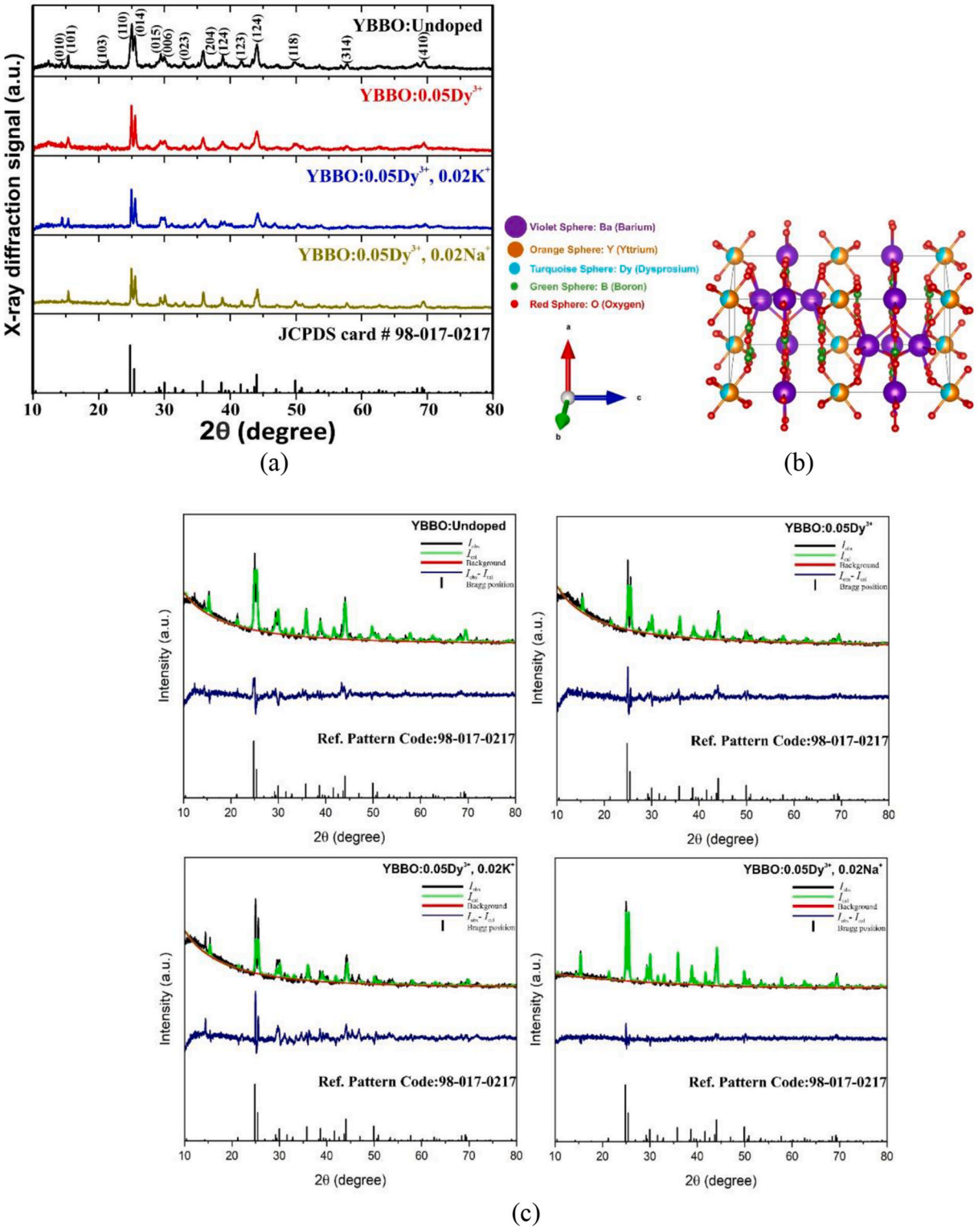

Fig. 1. **(a)** XRD patterns of undoped YBBO, YBBO:0.05Dy^{3+}, YBBO:0.05Dy^{3+},0.02 K^{+} and YBBO:0.05Dy^{3+},0.02Na^{+} samples along with the reference pattern (JCPDS card no. 98-017-0217). **(b)** Crystal structure representation of $YBa_3B_9O_{18}$ illustrating the atomic arrangement and coordination environments of Ba, Y/Dy, B, and O atoms. **(c)** Rietveld refinement profiles of the corresponding samples showing observed (black), calculated (green), background (red), and difference (blue) patterns, along with Bragg reflection positions. (For interpretation of the references to color in this figure legend, the reader is referred to the Web version of this article.)

Y^{3+} sites. Conversely, the large mismatch between Ba^{2+} and Dy^{3+} (~46.65%) excludes Ba sites as viable substitution positions.

Fig. 1c shows the Rietveld refinement results for all compositions based on the hexagonal *$P6_3/m$* structural model. The excellent agreement between observed and calculated patterns, along with low residuals, confirms the reliability of the structural model, refined using standard profile fitting with fixed occupancies and isotropic displacement parameters. The refinement quality indicators (Table 2) further support this, with R_p, R_{wp}, and χ^2 values remaining within acceptable limits typical for ceramic phosphor materials. Notably, the Dy^{3+}, K^{+} co-

Table 1
Ionic radius mismatch (D_r) between host cations (Ba^{2+}, Y^{3+}) and Dy^{3+} ions based on their coordination environments. The substitution feasibility is evaluated according to the radius difference criterion (<30%).

Ionic radius mismatch (D_r)	Ionic radius of the host cation (R_m)	Coordination number (CN)	Ionic radius of the doped cation (R_d)	Coordination number (CN)	Exchange Situation
	Ba^{2+}		**Dy^{3+}**		
46.65%	1.42	8	0.912	6	Not favorable for substitution
	Y^{3+}		**Dy^{3+}**		
12.22%	0.9	6	0.912	6	Favorable for substitution

Table 2
Refined lattice parameters, unit cell volume, and Rietveld refinement reliability factors (χ^2, R_p, R_{wp}, and R_{exp}) for undoped YBBO, Dy^{3+}-doped, and alkali co-doped samples.

YBBO				
Unit Cell	Undoped	0.05Dy^{3+}	0.05Dy^{3+}, 0.02 K^+	0.05Dy^{3+},0.05Na^+
a [Å]	7.18032	7.20031	7.14592	7.19207
b [Å]	7.18032	7.20031	7.14592	7.19207
c [Å]	17.13034	17.0961	17.00012	17.06743
α,β,γ [°]	90,90,120	90,90,120	90,90,120	90,90,120
Vol. [Å^3]	764.8637	767.5908	751.7948	764.5506
χ^2	1.4685	1.5292	1.9483	1.0345
R_p	0.0657	0.0657	0.0878	0.0556
R_{wp}	0.0846	0.0864	0.1159	0.0698
R_{exp}	0.0576	0.0565	0.0595	0.0675

Note: The refinement reliability factors are reported as absolute fractions rather than percentages. For example, $R_{wp} = 0.0846$ corresponds to 8.46%.

doped sample exhibits a slightly higher χ^2 and R-factors, suggesting increased lattice disorder compared to the Na^+ co-doped counterpart, which shows the best refinement quality among doped samples.

The refined lattice parameters summarized in Table 2 reveal subtle but systematic variations upon doping, confirming the sensitivity of the lattice to compositional modifications. The substitution of Y^{3+} (0.90 Å, CN = 6) with slightly larger Dy^{3+} ions (0.912 Å, CN = 6) leads to marginal lattice expansion in the Dy-only sample, as expected from the ionic size difference. However, co-doping with K^+ results in a contraction of lattice parameters and unit cell volume, suggesting enhanced local lattice distortion and charge compensation mechanisms that may introduce additional structural defects. In contrast, Na^+ co-doping maintains lattice parameters closer to the undoped structure, indicating a more compatible and less disruptive incorporation into the lattice. These contrasting lattice responses imply that Na^+ co-doping perturbs the host framework less severely than K^+, which may contribute to differences in luminescence efficiency and thermal stability discussed in subsequent sections.

To further support these structural observations, the crystallite size (*D*) and microstrain (ε) values were evaluated using multiple analytical approaches, including Debye–Scherrer, Williamson–Hall, Monshi–Scherrer, Halder–Wagner, and Size–Strain methods (Table 3) [35–38]. The results indicate that the crystallite size generally increases upon Dy^{3+} doping compared to the undoped sample, confirming improved crystallinity. For instance, the crystallite size calculated using the Williamson–Hall method increases from 45.83 nm (undoped) to 47.64 nm (Dy^{3+}-doped), while decreasing to 40.12 nm for the K^+ co-doped sample and remaining relatively higher at 44.02 nm for the Na^+ co-doped sample, supporting the observed trends in lattice distortion. However, a noticeable reduction in crystallite size is observed for the K^+ co-doped sample across most methods, suggesting increased lattice distortion and inhibited grain growth. In contrast, the Na^+ co-doped sample maintains relatively larger crystallite sizes, consistent with its more structurally compatible incorporation discussed above.

Similarly, the microstrain (ε) values exhibit a clear dependence on co-doping. The K^+ co-doped sample shows significantly higher strain values, particularly in the Halder–Wagner and Size–Strain models, indicating pronounced lattice distortion. On the other hand, the Na^+ co-doped sample presents comparatively lower strain values, reflecting a more relaxed lattice structure. The consistency of this trend across different analytical models further strengthens the conclusion that Na^+ co-doping introduces less structural perturbation than K^+.

Overall, the combined crystallite size and strain analysis corroborates the Rietveld refinement results, indicating that Na^+ co-doping preserves the average structural integrity of the $YBa_3B_9O_{18}$ host more effectively, whereas K^+ incorporation is associated with relatively higher lattice strain and structural disorder. These structural and microstructural variations may contribute to the observed differences in the optical and thermal behavior of the phosphors.

Taken together, the combined XRD, Rietveld refinement, and crystallite size–strain analyses support the preferential substitution of Dy^{3+} ions at Y^{3+} sites without detectable secondary-phase formation. Alkali co-doping influences the average lattice parameters, crystallite size, and microstrain, with K^+ co-doping producing a relatively more strained structure and Na^+ co-doping maintaining a comparatively lower-strain framework. These differences can be correlated with the observed variations in photoluminescence intensity, decay dynamics, and thermal stability. However, since the present structural evidence is mainly based on average XRD-derived parameters and size–strain analysis, the proposed relationship between lattice distortion and the local crystal-field environment around Dy^{3+} ions should be regarded as an indirect and comparative interpretation rather than direct proof of local coordination changes.

Accordingly, the higher strain and reduced crystallite size observed for the K^+ co-doped sample may indicate a greater degree of structural perturbation, whereas the lower strain observed for the Na^+ co-doped sample suggests a more structurally compatible incorporation. These differences are consistent with the changes observed in emission

Table 3
Crystallite size (*D*) and microstrain (ε) values of undoped and Dy^{3+}-doped YBBO phosphors with alkali co-doping, calculated using different analytical models.

Concentration		Undoped	0.05Dy^{3+}	0.05Dy^{3+},0.02 K^+	0.05Dy^{3+},0.02Na^+
Debye-Scherer	D (nm)	41.995	50.437	41.304	43.295
	$\delta\times10^{-3}$ (nm^{-2})	0.5670	0.3931	0.5861	0.5334
Williamson-Hall	D (nm)	45.8279	47.6369	40.1153	44.0171
	$\varepsilon \times 10^{-3}$	4.21	4.97	4.75	5.65
Monshi-Scherrer	D (nm)	39.0132	46.2245	38.5752	39.0214
	$\delta\times10^{-3}$ (nm^{-2})	0.6570	0.4680	0.6720	0.6567
Halder-Wagner	D (nm)	42.0168	43.1034	39.8406	41.4937
	$\varepsilon \times 10^{-3}$	18.9736	54.0370	38.4707	36.3318
Size-Strain	D (nm)	46.2672	47.9524	44.4222	45.5397
	$\varepsilon \times 10^{-3}$	4.1952	2.6832	7.6681	1.8973

intensity, lifetime behavior, chromaticity, and emission-derived effective Judd–Ofelt parameters. Nevertheless, direct confirmation of local symmetry changes would require additional local-structure probes such as EXAFS, detailed bond-length refinement, or site-symmetry analysis, which are beyond the scope of the present study.

3.2. Morphological and elemental analysis

Fig. 2a and b presents the EDX spectra and SEM micrographs of the undoped and Dy^{3+}-doped YBBO samples, respectively. The EDX analysis confirms the presence of the expected constituent elements, including Ba, Y, B, and O in the undoped sample, while the Dy^{3+}-doped sample additionally exhibits characteristic Dy peaks, verifying the successful incorporation of dopant ions into the host matrix. The absence of any extraneous elemental signals indicates high chemical purity, consistent with the XRD results.

Quantitative EDX data further reveal that the elemental composition is in reasonable agreement with the nominal stoichiometry, confirming the reliability of the synthesis process. Minor deviations in elemental percentages can be attributed to the inherent limitations of EDX analysis, particularly for light elements such as boron.

The SEM images show that both samples exhibit highly agglomerated and porous particle morphologies, which are characteristic of combustion-assisted synthesis. The observed agglomerates are composed of irregularly packed particles with rough surfaces and interconnected pores. However, because of the strong agglomeration, individual grain boundaries and reliable grain-size evolution cannot be clearly distinguished from the present SEM micrographs. Therefore, the SEM results are used mainly to describe the general morphology of the synthesized powders rather than to provide a quantitative grain-size analysis.

The Dy^{3+}-doped sample appears to show a more porous and rougher surface morphology compared with the undoped sample, suggesting that dopant incorporation may influence particle aggregation and microstructural development during synthesis. Nevertheless, this interpretation should be considered qualitative, since the present SEM images do not allow a direct demonstration of grain-growth evolution or a definitive morphology–photoluminescence relationship.

In phosphor materials, morphology can influence emission intensity through several factors, including light scattering, crystallinity, surface defect density, and the surface-area-to-volume ratio. In particular, an increased surface-area-to-volume ratio may promote surface defects and non-radiative recombination centers, which can reduce luminescence intensity. Similar morphology-dependent effects have been discussed in related phosphor systems [39–41]. In the present work, however, the PL enhancement is discussed primarily in relation to alkali-induced

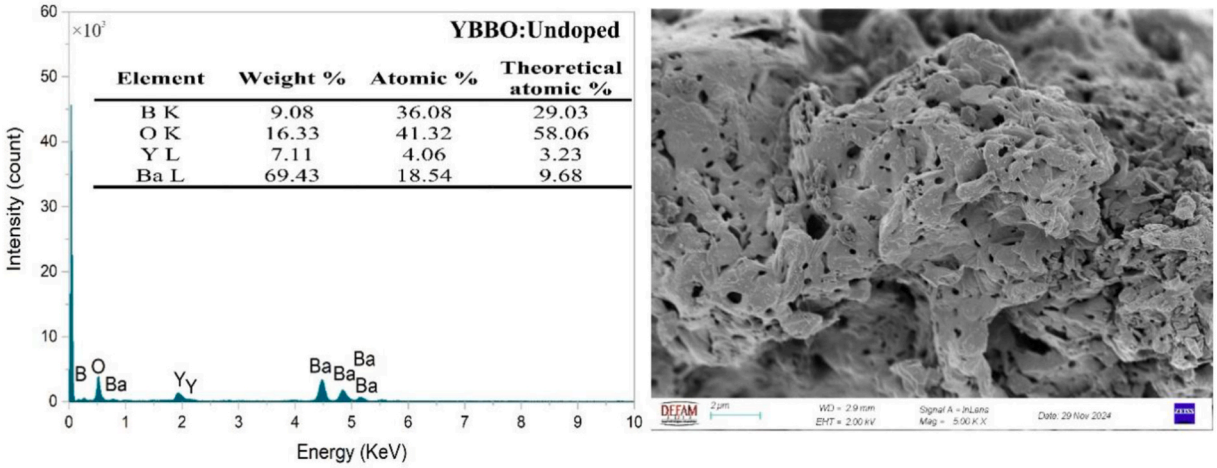

(a)

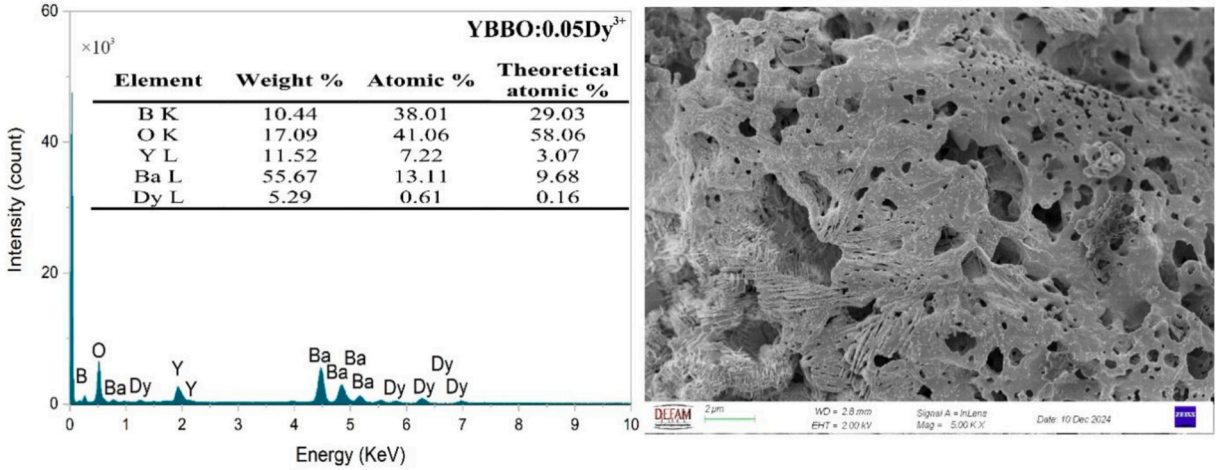

(b)

Fig. 2. **(a)** SEM micrograph of undoped YBBO with the corresponding EDX spectrum and quantitative elemental analysis shown in the inset. **(b)** SEM micrograph of YBBO:0.05Dy^{3+}, where the inset EDX spectrum confirms the presence of Dy^{3+} ions.

structural modification, defect regulation, and crystallinity/microstrain changes inferred from XRD and spectroscopic analyses. The SEM observations provide complementary qualitative support but are not used as direct proof of the morphology–PL relationship.

Moreover, the increased structural disorder observed in the doped sample is consistent with the lattice distortion inferred from the XRD analysis, further supporting the successful incorporation of Dy^{3+} ions into the host lattice.

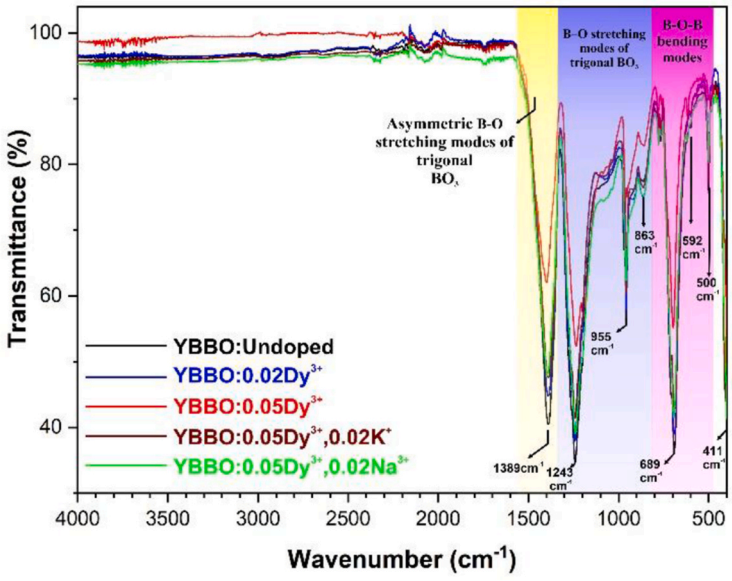

(a)

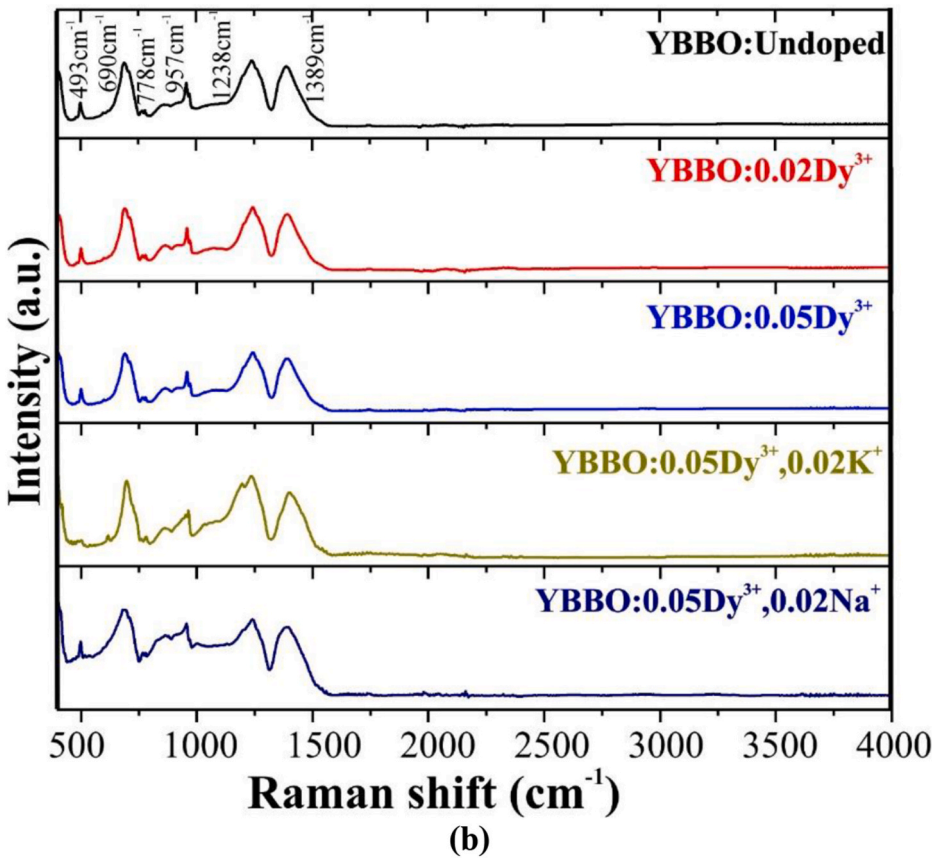

(b)

Fig. 3. (a) FTIR spectra of undoped YBBO, YBBO:0.02Dy^{3+}, YBBO:0.05Dy^{3+}, YBBO:0.05Dy^{3+},0.02 K^{+}, and YBBO:0.05Dy^{3+},0.02Na^{+} phosphors, showing characteristic vibrational bands of trigonal BO_3 units. (b) Raman spectra of the corresponding samples, confirming the borate framework through distinct vibrational modes associated with BO_3 groups.

The observed porous and agglomerated morphology can be attributed to the combustion-assisted synthesis process, during which the rapid release of gaseous by-products promotes the formation of loosely packed particle aggregates. The micrographs indicate that the larger secondary particles are composed of smaller crystallites, which is consistent with the crystallite sizes estimated from the XRD analysis. Such agreement between SEM and XRD results confirms the nanocrystalline nature of the synthesized phosphors. Furthermore, the EDS spectra reveal only the expected constituent elements without detectable impurity-related signals, indicating that the observed agglomeration is not associated with secondary phases but rather originates from the synthesis process itself. The homogeneous elemental distribution and high phase purity are also consistent with the XRD results.

3.3. FTIR and Raman analysis

The Fourier transform infrared (FTIR) spectra of undoped and Dy^{3+}-doped YBBO phosphors are presented in Fig. 3. The spectra exhibit well-defined absorption bands characteristic of borate-based materials, confirming the formation of the borate framework without the presence of extraneous phases. No additional impurity-related bands are observed, which is consistent with the phase purity confirmed by XRD analysis.

The prominent absorption band observed around 1398 cm^{-1} is attributed to the asymmetric stretching vibrations of B–O bonds in trigonal BO_3 units [42,43]. The bands located in the range of 800–1250 cm^{-1} (notably at 863, 955, and 1243 cm^{-1}) correspond to the symmetric stretching vibrations of BO_3 groups [44,45]. In the lower wavenumber region, the bands appearing at 500–700 cm^{-1} are assigned to B–O–B bending vibrations within the borate groups, reflecting the connectivity of the structural units [46]. Additionally, the weak band observed near 411 cm^{-1} is associated with Ln^{3+}–O lattice vibrations, indicating the interaction between rare-earth ions and the host lattice.

It is noteworthy that no vibrational features corresponding to tetrahedral BO_4 units are detected, further confirming that the structure is dominated by trigonal BO_3 units, in agreement with the crystallographic results obtained from XRD and Rietveld refinement. The observed FTIR band assignments are in good agreement with previously reported borate systems, particularly those reported by Peddaiah et al. [47] and Manhas et al. [48], thereby validating the structural integrity of the synthesized phosphors.

Only slight variations in band intensity and position are observed upon Dy^{3+} doping and alkali co-doping, suggesting that the incorporation of dopant ions induces minor local distortions without altering the fundamental borate framework. These subtle structural modifications may influence the local crystal field environment of Dy^{3+} ions, which is expected to play a role in the optical properties discussed in subsequent sections.

The Raman spectra of undoped and Dy^{3+}-doped YBBO phosphors are presented in Fig. 4. The spectra exhibit several well-defined vibrational modes characteristic of borate-based compounds, confirming the structural integrity of the host lattice. The observed Raman bands are consistent with the vibrational features of BO_3 structural units, in agreement with the FTIR results.

The prominent Raman bands located at ~493, 690, 778, 957, 1238, and 1389 cm^{-1} are attributed to various internal vibrational modes of trigonal BO_3 groups. In particular, the high-frequency band around 1389 cm^{-1} corresponds to the symmetric stretching vibrations of B–O bonds, while the bands in the range of 900–1250 cm^{-1} are associated with asymmetric stretching modes of BO_3 units. The lower wavenumber bands (below ~800 cm^{-1}) are assigned to bending and lattice vibrational modes of the borate framework [49–51].

Importantly, no Raman bands corresponding to tetrahedral BO_4 units are observed. The absence of distinct BO_4-related vibrational features, together with the known $YBa_3B_9O_{18}$ crystal structure, supports a framework composed exclusively of trigonal BO_3 units, consistent with both FTIR and XRD analyses, in agreement with previous reports [52–54].

Upon Dy^{3+} doping and alkali co-doping, no significant changes in peak positions are observed, indicating that the fundamental borate framework remains intact. However, slight variations in peak intensity and band broadening are noticeable, particularly for the co-doped samples, suggesting the introduction of local structural disorder and lattice distortion. Similar behavior has been widely reported in rare-earth-doped borate systems, where dopant incorporation primarily induces local lattice distortion and disorder, reflected by peak broadening and intensity variations, without altering the fundamental BO_3-based framework [55,56]. This behavior is consistent with the Rietveld refinement results and supports the notion that dopant incorporation induces subtle modifications in the local environment without altering the overall crystal symmetry.

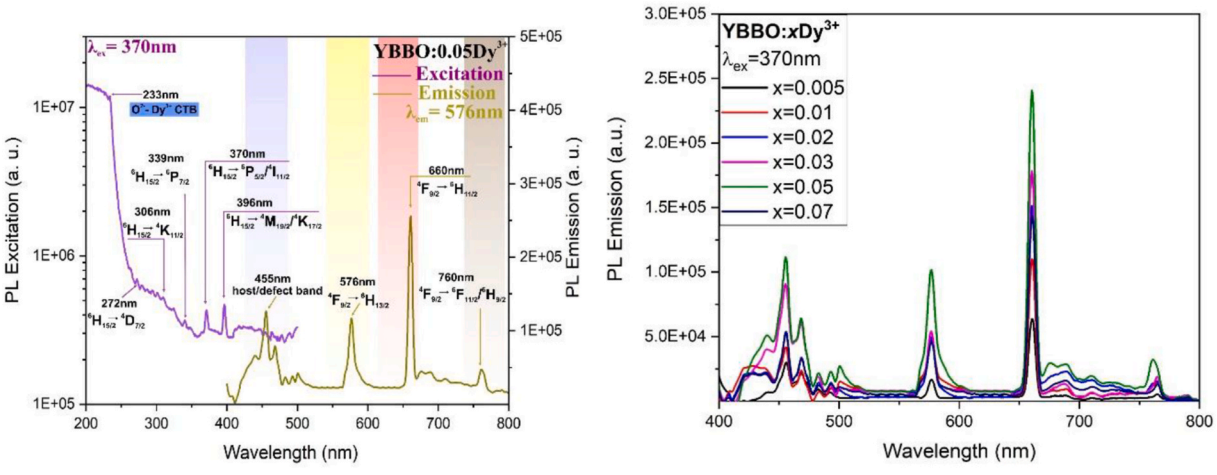

Fig. 4. (a) Photoluminescence excitation (λ_{em} = 576 nm) and emission (λ_{ex} = 370 nm) spectra of YBBO:0.05Dy^{3+} phosphor. (b) Emission spectra of YBBO:xDy^{3+} (x = 0.005–0.07) phosphors under 370 nm excitation. The broad feature around 455 nm is attributed to host-/defect-related emission rather than the conventional Dy^{3+} blue transition. Importantly, this band was not used for the quantitative thermal-quenching or activation-energy analysis. (For interpretation of the references to color in this figure legend, the reader is referred to the Web version of this article.)

These local structural perturbations may influence the crystal-field environment around Dy^{3+} ions and may contribute to the luminescence characteristics discussed in subsequent sections. The observed band broadening and slight shifts in co-doped samples are consistent with increased local structural disorder; however, these spectroscopic features should be considered complementary and indirect evidence rather than a direct determination of Dy^{3+} local coordination. Therefore, the FTIR/Raman results support a qualitative correlation between vibrational structure and optical behavior, but do not by themselves provide direct proof of local symmetry changes.

A clear correlation exists between the FTIR and Raman results. Both spectroscopic techniques consistently confirm that the YBBO structure is predominantly composed of trigonal BO_3 units. The FTIR bands associated with B–O stretching and B–O–B bending vibrations correspond well with the Raman-active vibrational modes observed in similar spectral regions. Moreover, the absence of characteristic BO_4-related features in both spectra further supports the crystallographic model obtained from XRD and Rietveld refinement. The slight variations in peak intensity and band broadening observed after Dy^{3+} and alkali co-doping indicate local structural distortion within the borate framework. These observations are in good agreement with the lattice strain and crystallite-size variations obtained from XRD analysis and provide complementary evidence that alkali incorporation modifies the local crystal-field environment around Dy^{3+} ions, ultimately influencing their luminescence properties.

4. Photoluminescence measurements

4.1. Photoluminescence excitation and emission characteristics of Dy^{3+} ions

The excitation spectrum of YBBO:0.05Dy^{3+} monitored at 576 nm ($^4F_{9/2} \rightarrow {}^6H_{13/2}$) consists of several sharp lines assigned to f–f transitions from the $^6H_{15/2}$ ground state to higher-lying Dy^{3+} levels (Fig. 4a), confirming efficient intra-4f excitation of Dy^{3+} under near-UV illumination (typically in the 340–380 nm range), as commonly reported in Dy^{3+}-activated phosphors such as CLSPO:Dy^{3+} and $Gd_2Si_2O_7$:Dy^{3+} [18,57,58]. The presence of multiple well-resolved excitation bands indicates that Dy^{3+} ions occupy well-defined lattice sites with a relatively ordered local crystal field, consistent with the structural analysis showing preferential substitution at Y^{3+} octahedral sites. The observed excitation bands are also consistent with those reported for Dy^{3+}-doped phosphate glasses, where several excitation transitions originating from the $^6H_{15/2}$ ground state were observed in the near-UV region. Although the host structures are different, the similarity of the excitation features suggests that the excitation process is primarily governed by the intrinsic 4f–4f transitions of Dy^{3+} ions and further supports the suitability of near-UV excitation for efficient luminescence generation in Dy^{3+}-activated materials [11].This excitation profile further demonstrates that YBBO:Dy^{3+} can be effectively pumped by near-UV/blue LED chips used in pc-WLEDs [59]. These excitation features translate into a distinct emission behavior in YBBO:Dy^{3+} under near-UV excitation.

Under 370 nm excitation, the emission spectrum of YBBO:0.05Dy^{3+} shows three sharp Dy^{3+} *4f–4f* bands centered at 576, 660 and 760 nm, which can be assigned to the $^4F_{9/2} \rightarrow {}^6H_{13/2}$ (yellow), $^4F_{9/2} \rightarrow {}^6H_{11/2}$ (red), and $^4F_{9/2} \rightarrow {}^6H_{9/2}/{}^6F_{11/2}$ (deep-red) transitions, respectively [60–62]. No distinct blue emission band corresponding to the $^4F_{9/2} \rightarrow {}^6H_{15/2}$ transition of Dy^{3+} is observed in the 470–500 nm region, indicating suppression of this transition in the YBBO host. A distinct emission band centered at ~455 nm is observed, which is attributed to host-related or defect-induced emission rather than intrinsic Dy^{3+} transitions. The absence of secondary phases in the XRD patterns suggests that this band is unlikely to originate from impurity phases. Similar broad blue–visible emissions associated with intrinsic host defects, oxygen-related defect centers, or self-trapped exciton (STE)-like states have been reported in borate and related oxide hosts [46,63–65]. Therefore, the ~455 nm band is tentatively assigned to intrinsic host-/defect-related luminescence within the YBBO lattice. These defect-related centers can act both as independent emitters and as intermediate states in host-to-Dy^{3+} energy-transfer processes, which naturally couples their concentration-quenching behavior to that of the Dy^{3+} emission. The concentration dependence of the ~455 nm band follows a trend similar to that of the Dy^{3+} emission. Such behavior can be explained by the interaction between host-/defect-related excited states and Dy^{3+} ions through host-sensitized or defect-assisted energy-transfer processes, as reported in Dy^{3+}-containing borate and related systems [66–68]. In the present system, Dy^{3+} incorporation may influence both the defect population and the host-to-Dy^{3+} energy-transfer pathways. At higher Dy^{3+} concentrations, enhanced Dy^{3+}–Dy^{3+} interactions together with defect-assisted non-radiative relaxation channels can simultaneously suppress both the host-related emission and the Dy^{3+} emission, resulting in comparable concentration-quenching behavior.

The 660 nm line is 4.14 times more intense than the 576 nm band ($I_{660}/I_{576} \approx 4.14$), indicating a relatively strong red emission compared to typical Dy^{3+} phosphors; this unusual dominance of the 660 nm transition ($I_{660}/I_{576} \approx 4.14$) anticipates the redistribution of radiative transition strengths toward higher-rank components, as later confirmed by the Judd–Ofelt analysis. The 760 nm band appears as a weaker shoulder, suggesting a secondary contribution from deep-red emission channels.

Dy^{3+} from the $^4F_{9/2}$ excited state typically exhibits four characteristic emission bands located at ~480, 575, 660 and ~750 nm, which are widely recognize d as the canonical $^4F_{9/2} \rightarrow {}^6H_j$ transitions in Dy^{3+}-activated phosphors, with their relative intensities being strongly host dependent. The yellow $^4F_{9/2} \rightarrow {}^6H_{13/2}$ transition is a hypersensitive electric-dipole line that is strongly enhanced at low-symmetry, non-centrosymmetric sites, whereas the blue $^4F_{9/2} \rightarrow {}^6H_{15/2}$ line is a magnetic-dipole transition favored at more symmetric environments [57,60]. This behavior follows the well-established yellow-to-blue (Y/B) intensity ratio criterion commonly used to probe the local symmetry around Dy^{3+} ions. In rare-earth-doped phosphors, electric-dipole (ED) transitions are generally more intense than magnetic-dipole (MD) transitions. According to Judd–Ofelt theory, ED transitions become partially allowed through crystal-field-induced mixing with opposite-parity electronic configurations, resulting in enhanced oscillator strengths and radiative transition probabilities. Since the magnitude of this mixing depends strongly on the local symmetry and crystal-field environment surrounding the activator ion, ED transitions are highly sensitive to structural distortion and site asymmetry. In contrast, MD transitions are largely determined by the free-ion electronic structure and are therefore comparatively insensitive to the host lattice. Consequently, local symmetry reduction and crystal-field perturbation commonly lead to stronger ED emission relative to MD emission in rare-earth-activated phosphors [69–71]. Several hosts also show well-resolved red ($^4F_{9/2} \rightarrow {}^6H_{11/2}$) and deep-red ($^4F_{9/2} \rightarrow {}^6H_{9/2}/{}^6F_{11/2}$) bands at ~660 and ~750 nm with variable intensity ratios to yellow and blue, depending on crystal field strength, site symmetry and multipolar Dy–Dy interactions [61,72]. In YBBO:Dy^{3+}, the suppression of the blue emission band together with a strong 660 nm line and weaker 576 and 760 nm lines indicates that the local field around Dy^{3+} and intra-ionic relaxation pathways may preferentially populate red-emitting channels, resulting in a yellow–red–biased spectrum rather than the typical blue–yellow white emission. This unusual emission distribution may be associated with changes in the local crystal-field environment induced by structural distortion, as indirectly inferred from the XRD and strain analysis. The suppression of the conventional Dy^{3+} blue transition and enhancement of the red emission suggest possible changes in local asymmetry and electric-dipole contribution. This interpretation is further supported, in a comparative sense, by the emission-derived effective Judd–Ofelt parameters discussed in Section 4.6.

Fig. 4b shows the emission spectra of YBBO:$x$$Dy^{3+}$ (x = 0.005–0.07)

phosphors under 370 nm excitation. All samples exhibit identical sets of characteristic Dy^{3+} emission bands without any noticeable peak shift, indicating that the local coordination environment of Dy^{3+} ions remains unchanged with increasing concentration. The emission intensity increases with Dy^{3+} concentration and reaches a maximum at $x = 0.05$. A further increase to $x = 0.07$ results in a pronounced decrease in intensity, indicating the onset of concentration quenching. This behavior is attributed to enhanced Dy–Dy energy transfer at higher concentrations, which promotes non-radiative processes such as cross-relaxation and multipolar interactions, as commonly reported for rare-earth activated phosphors [73–75]. Therefore, the optimal Dy^{3+} concentration for achieving maximum emission in the YBBO host is determined to be $x = 0.05$, and this composition is selected for subsequent photoluminescence investigations.

Interestingly, the intensity of the ~455 nm host-related emission band follows a similar concentration-dependent trend as the Dy^{3+} 4f–4f emission, with both reaching a maximum at $x = 0.05$. This correlation indicates that the 455 nm band is associated with defect or host-related states whose population and radiative efficiency are modulated by Dy^{3+} incorporation. This behavior is most likely governed by defect formation and charge-compensation processes induced by Dy^{3+} doping, together with possible host-to-Dy^{3+} energy transfer [46,76–78]. At higher Dy^{3+} concentrations, enhanced Dy^{3+}–Dy^{3+} interactions and defect-assisted non-radiative pathways lead to simultaneous concentration quenching of both the host-related and Dy^{3+} emissions.

To gain further insight into the mechanism responsible for concentration quenching, the critical distance (R_c) between Dy^{3+} ions was evaluated using the Blasse approach, which provides an estimate of the average separation between activator ions at the quenching concentration. The critical distance can be expressed as [79]:

$$R_c \approx 2\left[\frac{3V}{4\pi x_c N}\right]^{1/3} \quad (1)$$

where V represents the unit cell volume, x_c is the critical Dy^{3+} concentration corresponding to maximum emission intensity, and N denotes the number of formula units per unit cell. Using the refined structural parameters ($V \approx 767.59$ Å^3), $x_c = 0.05$, and $N = 4$ for the hexagonal YBBO lattice, the critical distance was calculated to be approximately 8.8 Å.

This value significantly exceeds the typical threshold (~5 Å) associated with exchange interactions, indicating that short-range exchange coupling is unlikely to be the dominant mechanism governing concentration quenching [79]. Instead, the energy transfer between Dy^{3+} ions is more plausibly mediated by long-range multipolar interactions. This interpretation is consistent with the gradual decrease in emission intensity beyond the optimum concentration ($x = 0.05$), which is characteristic of multipolar interaction–driven quenching behavior [1,80,81].

The relatively high optimum Dy^{3+} concentration (~5 wt%) observed in the YBBO:xDy^{3+} system is consistent with behavior reported for several Dy^{3+}-activated phosphors, where concentration quenching is governed by long-range multipolar interactions rather than short-range exchange mechanisms [82,83]. In such systems, optimum concentrations in the range of 2–7 mol% or wt% are commonly associated with weak activator–activator interactions and gradual quenching behavior [84].

In the present case, the calculated critical distance ($R_c \approx 8.8$ Å) exceeds the typical threshold (~5 Å) for exchange interactions, further supporting the dominance of multipolar energy transfer [2].

Taken together, the relatively high optimum concentration, large critical distance, and smooth quenching behavior consistently indicate that non-radiative energy transfer in YBBO:Dy^{3+} is dominated by long-range multipolar interactions. Due to the limited number of data points beyond the optimal concentration ($x = 0.05$), the Dexter–Van Uitert model was not applied, as reliable fitting requires multiple points in the quenching region.

4.2. Effect of alkali Co-doping on the photoluminescence properties of YBBO:Dy^{3+}

The influence of alkali ion co-doping on the photoluminescence behavior of YBBO:Dy^{3+} phosphors was systematically investigated by introducing Na^+ and K^+ ions into the optimized composition ($x = 0.05$ Dy^{3+}). Fig. 5a and b presents the emission spectra of YBBO:0.05Dy^{3+}, $y$$K^+$ and YBBO:0.05Dy^{3+},$y$$Na^+$ samples under 370 nm excitation. In all cases, the characteristic Dy^{3+} emission bands – the yellow ($^4F_{9/2} \rightarrow {}^6H_{13/2}$) and red ($^4F_{9/2} \rightarrow {}^6H_{11/2}$) transitions discussed in Section 4.1- remain unchanged in position, indicating that alkali co-doping does not alter the fundamental crystal structure or the substitutional site of Dy^{3+} ions. However, a significant enhancement in emission intensity is observed, demonstrating the critical role of alkali ions in modulating the luminescence efficiency.

For K^+ co-doping, the emission intensity initially increases with increasing K^+ concentration and reaches a maximum at $y = 0.02$, yielding an enhancement of approximately (based on the dominant 660 nm emission band) 1.4-fold compared to the singly doped YBBO:Dy^{3+} phosphor. In contrast, Na^+ co-doping results in a more pronounced improvement, with the optimal composition ($y = 0.02$) exhibiting an enhancement of approximately 1.8-fold (I_{660} enhancement). This difference clearly indicates that Na^+ is more effective than K^+ in enhancing the luminescence performance of the YBBO:Dy^{3+} system.

The observed enhancement may arise from several synergistic effects induced by alkali-ion incorporation. First, the introduction of monovalent Na^+ and K^+ ions may modify the structural environment of the $YBa_3B_9O_{18}$ host through charge-compensation effects, defect regulation, and lattice-strain variation. Such modifications can influence the local crystal-field environment around Dy^{3+} ions and may affect the relative strength of electric-dipole emission transitions. Second, alkali ions can contribute to the reduction of defect-assisted non-radiative recombination centers, thereby improving the overall emission efficiency. Third, alkali incorporation may influence host-to-activator interactions and defect-assisted energy-transfer pathways. However, these interpretations should be considered indirect and comparative, since direct local-structure probes were not performed in the present study.

The crystallite-size and microstrain analyses (Table 3) reveal that Na^+ and K^+ co-doping alter the crystal-growth behavior and average lattice structure of $YBa_3B_9O_{18}$. Similar behavior was reported by Yadav et al. in alkali-ion-modified rare-earth phosphors, where Li^+, Na^+, and K^+ incorporation enhanced luminescence through combined effects of crystal-field modification and morphology control [85]. Furthermore, the comprehensive review by Yadav et al. [86] emphasized that morphology engineering, crystallinity, particle size, and local symmetry are key factors governing the optical performance of rare-earth-doped phosphors. Singh et al. also demonstrated that alkali-ion co-doping in Eu^{3+}-activated phosphors can improve crystallite growth, reduce structural defects, and enhance emission intensity through combined structural and crystal-field effects [87].

Previous studies on alkali-ion-modified Dy^{3+}-activated phosphors have also shown that Li^+/Na^+/K^+ co-doping can enhance luminescence through combined effects of charge compensation, defect regulation, crystallinity improvement, lattice-strain modification, and changes in crystal-field-related emission behavior [3,4,88–90]. In several Dy^{3+}-activated oxide and borate-related hosts, Na^+ or Li^+ co-doping has been reported to provide more favorable emission enhancement than K^+, which was attributed to reduced defect-assisted non-radiative relaxation and a better balance between structural compatibility and radiative emission efficiency [3,4,88]. Similar trends have also been reported for Eu^{3+}-activated phosphors, where alkali co-doping modifies local symmetry and electric-dipole transition probabilities, leading to enhanced emission intensity and improved optical performance [28,77,91].

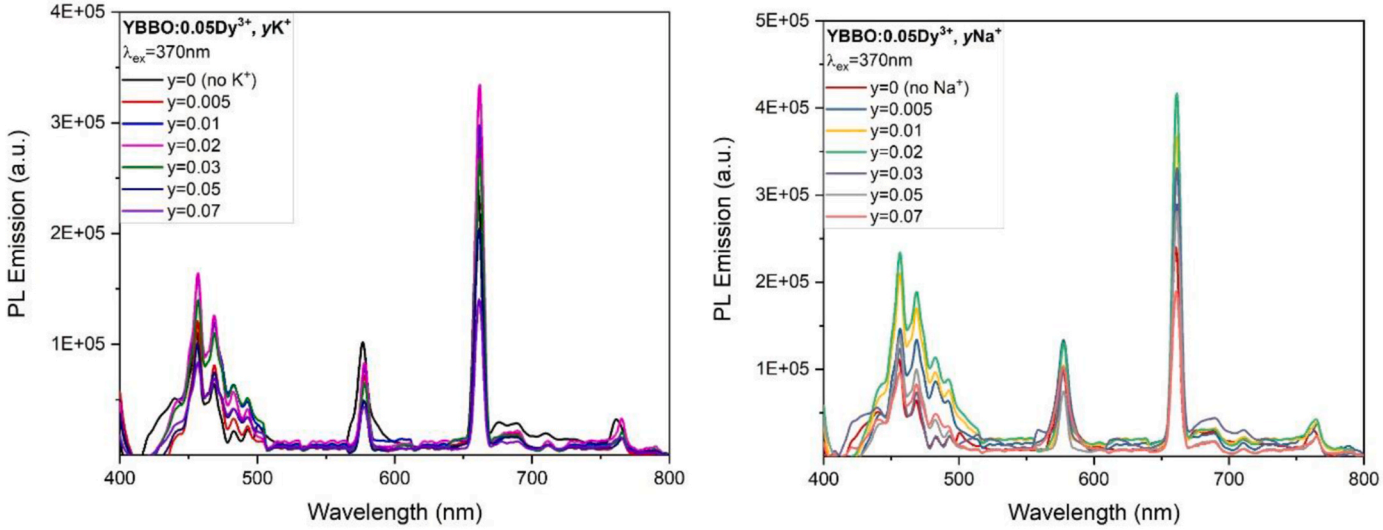

Fig. 5. Emission spectra of (a) YBBO:0.05Dy^{3+},yK^{+} and (b) YBBO:0.05Dy^{3+},yNa^{+} phosphors (y = 0–0.07) under 370 nm excitation.

In this context, the stronger microstrain observed for K^{+}-co-doped $YBa_3B_9O_{18}$:Dy^{3+} and the superior luminescence enhancement obtained with Na^{+} co-doping are consistent with the broader literature showing that stronger lattice perturbation does not necessarily produce the highest total emission intensity. Excessive lattice distortion may introduce additional disorder and defect-assisted non-radiative losses, whereas moderate alkali-induced structural modification can provide a more favorable balance between radiative and non-radiative processes. Therefore, the higher enhancement efficiency of Na^{+} compared with K^{+} is interpreted as being consistent with more favorable structural compatibility and reduced non-radiative losses, rather than as direct proof of a specific local symmetry change.

The variation in the intensity ratio (I_{660}/I_{576}), which is ~4.0 for K^{+} and ~3.17 for Na^{+} co-doped samples, further suggests that the two alkali ions modify the relative emission distribution of Dy^{3+} differently. The higher I_{660}/I_{576} ratio in the K^{+} co-doped sample is consistent with stronger structural perturbation inferred from the microstrain analysis, while the higher total emission intensity of the Na^{+} co-doped sample suggests a more favorable balance between radiative emission and defect-assisted non-radiative relaxation. Nevertheless, because direct local-structure probes such as EXAFS, detailed bond-length refinement, or site-symmetry analysis were not performed, the relationship between alkali-induced local asymmetry and radiative behavior is discussed here as a literature-supported qualitative interpretation rather than direct experimental proof.

At higher alkali concentrations ($y > 0.02$), a decrease in emission intensity is observed for both Na^{+} and K^{+} co-doped samples. This behavior is attributed to the onset of concentration quenching associated with excessive lattice distortion and increased probability of non-radiative energy transfer processes.

Overall, the results demonstrate that alkali-ion co-doping is an effective strategy for enhancing the photoluminescence performance of YBBO:Dy^{3+} phosphors, with Na^{+} exhibiting superior performance compared to K^{+}. These findings highlight the strong correlation between local structural distortion, crystal-field modification, and luminescence efficiency in borate-based phosphor systems.

4.3. Temperature-dependent photoluminescence and thermal stability

The temperature-dependent photoluminescence (PL) properties of YBBO:0.05Dy^{3+} and alkali co-doped samples were investigated in the range of 300–550 K (Fig. 6). For all samples, the emission intensity of the Dy^{3+} band at ~660 nm gradually decreases with increasing temperature, indicating the presence of thermally activated non-radiative processes. Before this analysis, the wavelength scale and emission-band assignments were carefully rechecked, and no systematic wavelength displacement was observed. The decrease in PL intensity with increasing temperature can be reasonably attributed to enhanced lattice vibrations and phonon-assisted non-radiative relaxation processes, as commonly reported for rare-earth-doped phosphors. At elevated temperatures, the interaction between Dy^{3+} excited states and host-lattice phonons becomes stronger, which increases the probability of multiphonon relaxation and thermally activated crossover from the excited state to non-radiative pathways. As a result, fewer excited Dy^{3+} ions return radiatively to the ground state, leading to thermal quenching of the emission intensity. This behavior is consistent with previous reports on Er^{3+}/Yb^{3+}/Li^{+} and Ho^{3+}/Yb^{3+}/Bi^{3+} co-doped $ZnGa_2O_4$ phosphors, where the emission intensity decreases progressively with increasing temperature because enhanced lattice vibrations and electron–phonon interactions promote non-radiative relaxation processes [92,93]. Similar phonon-assisted thermal quenching mechanisms have also been reported for Tm^{3+}/Yb^{3+}/Mg_4^{2+} phosphors through temperature-dependent luminescence investigations [94]. The singly doped YBBO:0.05Dy^{3+} sample exhibits a relatively rapid decrease in PL intensity, retaining only ~23% of its initial intensity at 550 K. This behavior suggests that thermally activated non-radiative relaxation becomes more pronounced at elevated temperatures, most likely through enhanced electron–phonon interaction and multiphonon relaxation pathways.

In contrast, the alkali co-doped samples show improved PL retention at elevated temperatures compared with the singly doped YBBO:0.05Dy^{3+} sample. The K^{+} co-doped sample maintains ~40% of its initial intensity at 550 K, while the Na^{+} co-doped sample retains approximately 40–42%, indicating a moderate improvement in thermal-quenching resistance. This improvement may be associated with alkali-induced modification of the defect environment and average lattice structure, as suggested by the XRD-derived microstructural trends discussed in Section 3. However, the present data do not directly prove a one-to-one relationship between reduced microstrain, increased structural rigidity, suppressed phonon-assisted relaxation, and enhanced thermal stability. Therefore, this relationship is discussed as a probable and literature-supported interpretation rather than direct experimental proof of a specific microscopic quenching pathway.

Furthermore, the more gradual decrease in intensity for the co-doped samples suggests a lower probability of thermally activated quenching compared with the singly doped sample. This tendency may be related to

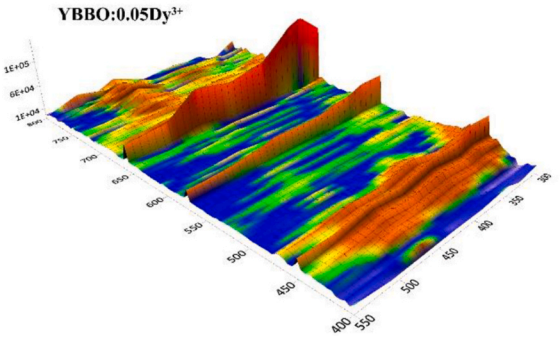

(a)

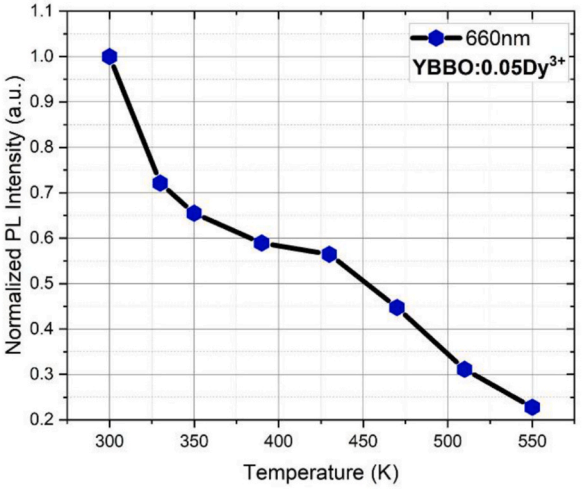

(b)

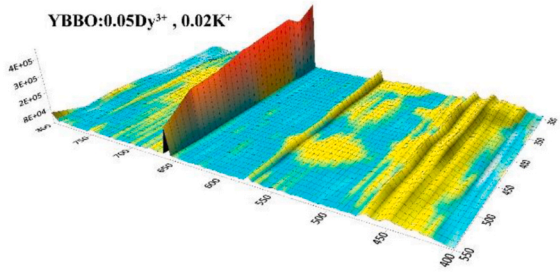

(c)

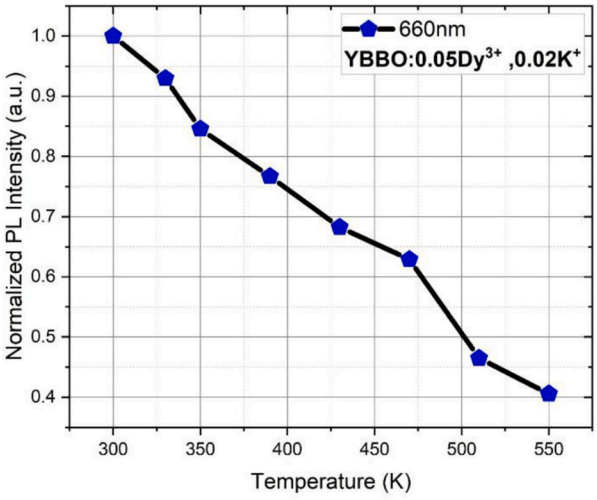

(d)

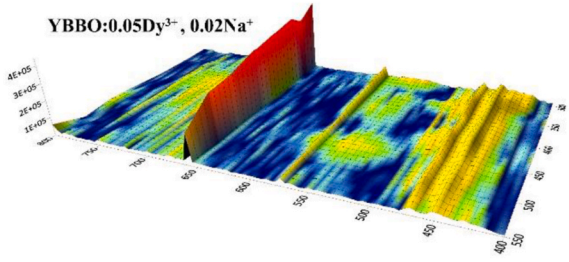

(e)

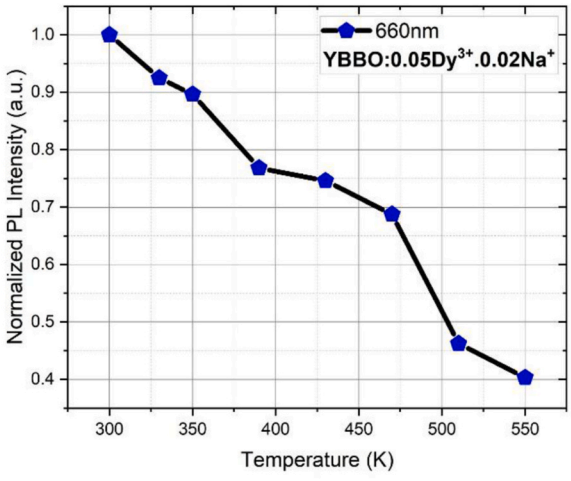

(f)

Fig. 6. Temperature-dependent photoluminescence behavior of YBBO:0.05Dy^{3+}, YBBO:0.05Dy^{3+}, 0.02 K^{+}, and YBBO:0.05Dy^{3+}, 0.02Na^{+}. Emission contour maps are shown in (a), (c), and (e), while the corresponding normalized PL intensity at 660 nm as a function of temperature is presented in (b), (d), and (f), respectively.

a more favorable defect environment and local lattice modification, which could reduce defect-assisted non-radiative recombination and phonon-assisted energy dissipation. Nevertheless, direct measurements of defect density, phonon coupling, or Dy^{3+} local coordination would be required to confirm this mechanism.

Overall, alkali co-doping improves the high-temperature PL retention of YBBO^{3+} phosphors, with Na^+ and K^+ showing comparable thermal-quenching behavior and both outperforming the singly doped system. The proposed mechanism is based on indirect structural and spectroscopic evidence and is therefore presented as a plausible interpretation supported by literature.

4.4. Thermal quenching analysis and activation energy

The thermal quenching behavior was further analyzed using the Arrhenius model, as presented in Fig. 7a and b. The activation energies (ΔE) were determined from the slopes of the linear fits of $\ln[(I/I_0)^{-1} - 1]$ versus $1/kT$ and were found to be 0.189 ± 0.009 eV for the K^+ co-doped sample and 0.202 ± 0.013 eV for the Na^+ co-doped sample. The slightly higher ΔE value obtained for the Na^+ co-doped phosphor indicates a stronger resistance to thermal quenching. The slightly higher activation energy of the Na^+ co-doped sample may be associated with a more favorable defect environment and less disruptive lattice modification, as inferred from the average structural and microstructural analyses. However, since direct measurements of local defect density, phonon coupling, or Dy^{3+} site symmetry were not performed, this interpretation should be regarded as indirect and literature-supported rather than direct experimental proof.

In contrast, the larger ionic radius of K^+ may induce relatively higher lattice distortion, resulting in a comparatively lower activation energy. Overall, these results demonstrate that alkali co-doping significantly improves the thermal stability of YBBO:Dy^{3+} phosphors, with Na^+ providing a more favorable effect than K^+.

Our sample exhibits competitive thermal robustness when benchmarked against recent Dy^{3+}-activated borate and tungstate phosphors designed for high-temperature operation. In the borate family, Dy^{3+}-doped $LaMgB_5O_{10}$ shows an activation energy of 0.1975 eV for thermal quenching, indicating reasonable stability at elevated temperatures [95]. Highly thermostable $Ba(ZnBO_3)PO_4$:Dy^{3+} retains 88% of its room-temperature emission at 473 K, while Ca_2MgWO_6:Dy^{3+} exhibits an activation energy of ~0.21 eV and a high quenching temperature (~499 K) [81,96]. Furthermore, $Li_3Ba_2Gd_3(WO_4)_8$:Dy^{3+} shows excellent thermal stability with an activation energy of ~0.35 eV [19].

In comparison, the present YBBO:Dy^{3+} phosphors retain approximately 40-42% (Na^+) and ~40% (K^+) of their initial emission intensity at 550 K, with corresponding activation energies of 0.202 ± 0.013 eV and 0.189 ± 0.009 eV, respectively. These values are comparable to several thermally stable Dy^{3+}-doped borate and tungstate hosts reported in the literature. Notably, the present evaluation at 550 K represents a relatively stringent condition compared to many previous studies conducted at lower temperatures. Although the activation energies do not reach the highest reported values, the obtained thermal stability is sufficient for practical high-power pc-WLED applications. Furthermore, the co-doped samples exhibit markedly improved thermal stability compared with the singly doped YBBO:Dy^{3+} phosphor, which retains only ~23% of its initial emission intensity at 550 K.

4.5. Luminescence decay dynamics and lifetime analysis

The luminescence decay behavior of Dy^{3+} ions in YBBO phosphors was investigated to evaluate the overall excited-state relaxation dynamics and the influence of alkali co-doping on the Dy^{3+} emission behavior. Fig. 8 shows the decay curves of YBBO:xDy^{3+} ($x = 0.02$ and 0.05) and alkali co-doped YBBO:0.05Dy^{3+},0.02 K^+ and YBBO:0.05Dy^{3+},0.02Na^+ samples monitored at the characteristic Dy^{3+} $^4F_{9/2} \rightarrow {}^6H_{13/2}$ emission band at ~576 nm, while the corresponding fitting parameters are summarized in Table 4.

The decay profiles exhibit non-single-exponential behavior, indicating the presence of multiple relaxation components that may arise from slightly different Dy^{3+} local environments and defect-associated relaxation channels. The decay curves were fitted using a multi-exponential function of the form:

$$I(t) = A_1\, exp(-t/\tau_1) + A_2\, exp(-t/\tau_2) + A_3\, exp(-t/\tau_3) \quad (2)$$

where A_i and τ_i represent the relative amplitudes and lifetimes of each decay component, respectively. The average lifetime (τ_{avg}) was calculated using a weighted expression based on these parameters. The χ^2 values close to unity further confirm the reliability of the fitting.

To evaluate the suitability of the fitting model, the decay curve of the YBBO:0.05Dy^{3+} phosphor was additionally fitted using a bi-exponential function and compared with the tri-exponential model. The bi-exponential fit yielded a χ^2 value of 1.18, whereas the tri-exponential fit resulted in a lower χ^2 value of 1.07, indicating a better representation of the experimental decay profile. This result suggests that an

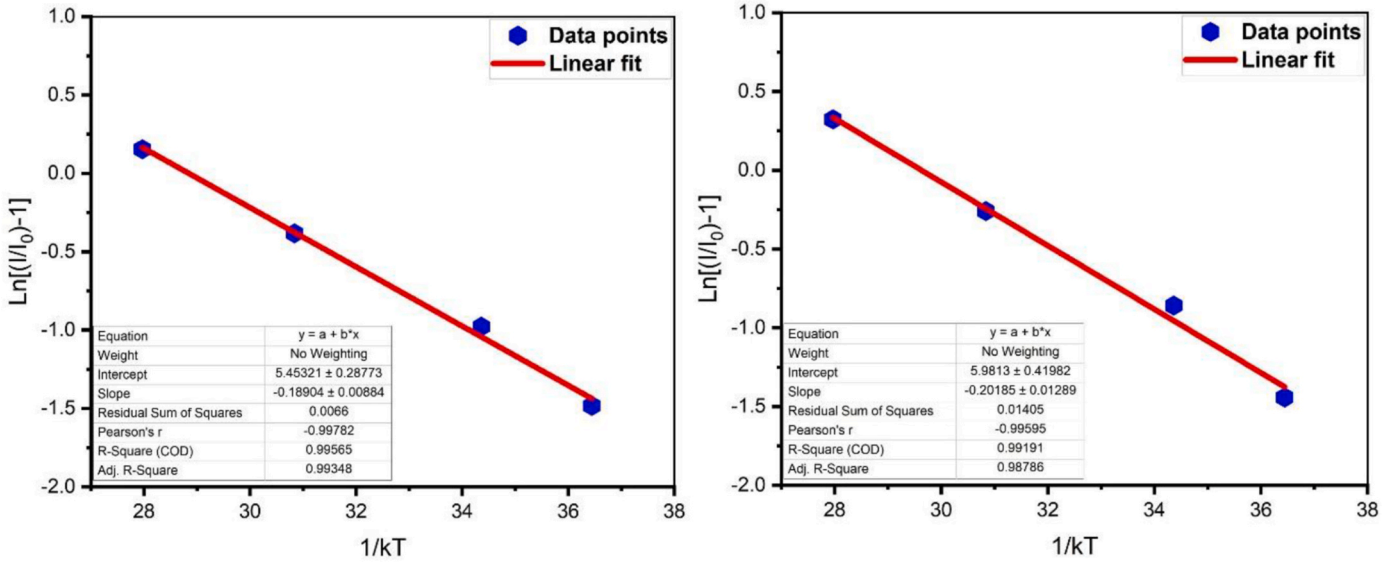

Fig. 7. Arrhenius plots of $\ln[(I/I_0)^{-1} - 1]$ versus 1/kT for **(a)** YBBO:0.05Dy^{3+},0.02 K^+ and **(b)** YBBO:0.05Dy^{3+},0.02Na^+ phosphors.

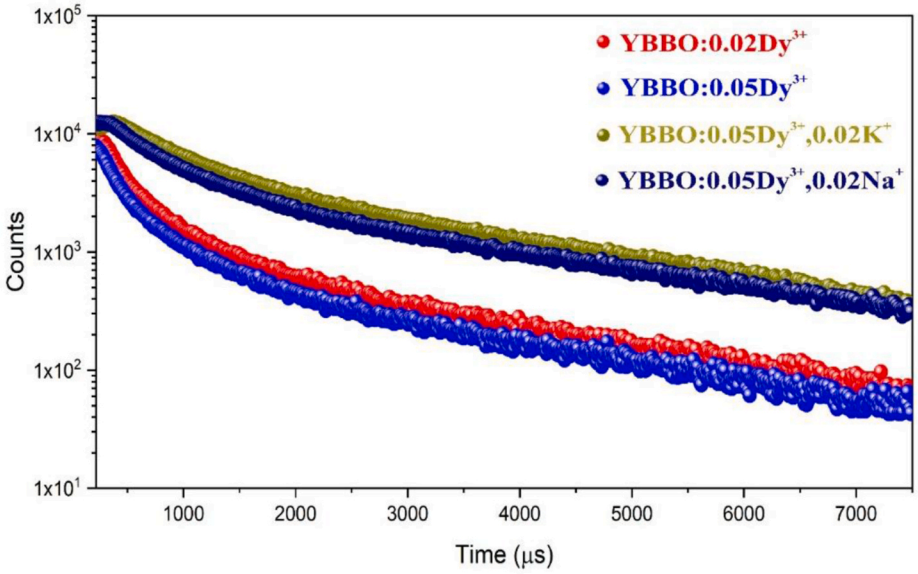

Fig. 8. Photoluminescence decay curves of YBBO:xDy^{3+} (x = 0.02 and 0.05) and alkali co-doped YBBO:0.05Dy^{3+},0.02 K^{+} and YBBO:0.05Dy^{3+},0.02Na $^{+}$ phosphors monitored at the Dy^{3+} $^{4}F_{9/2} \rightarrow {}^{6}H_{13/2}$ emission band at ~576 nm under 370 nm excitation.

Table 4
Multi-exponential fitting parameters (τ_1, τ_2, τ_3), relative contributions (Rel.%), average lifetimes (τ_{avg}), and goodness-of-fit values (χ^2) for YBBO:xDy^{3+} and alkali co-doped YBBO:0.05Dy^{3+} phosphors under 370 nm excitation.

		Time(μs)	Rel.%	τ_{avg}(ms)	χ^2
YBBO:0.02Dy^{3+}	τ_1	20.728	43.43	1263.831	1.1128
	τ_2	1359.268	56.57		
YBBO:0.05Dy^{3+}	**τ_1**	12.592	20.57	1528.331	1.0700
	τ_2	460.340	34.09		
	τ_3	2400.092	45.34		
YBBO:0.05Dy^{3+},0.02K^{+}	**τ_1**	497.228	28.78	2117.446	1.1209
	τ_2	2772.068	71.22		
YBBO:0.05Dy^{3+},0.02Na^{+}	**τ_1**	424.132	35.45	1646.494	1.1275
	τ_2	2287.064	64.55		

additional slow decay component contributes to the luminescence decay behavior of Dy^{3+} ions in the YBBO lattice. Therefore, the tri-exponential model was retained for the lifetime analysis. Nevertheless, the discussion focuses primarily on the average lifetime (τ_{avg}), which provides a more robust representation of the overall decay behavior than the individual lifetime components.

The multi-exponential decay behavior suggests that Dy^{3+} ions may experience slightly different local environments within the host lattice, possibly due to lattice disorder and defect-associated relaxation processes. This interpretation is consistent with structural distortions indirectly inferred from XRD analysis. Importantly, the broad ~455 nm band is assigned to host-/defect-related emission and was not used as evidence for the Dy^{3+} lifetime behavior. As listed in Table 4, the average lifetime increases from 1263.8 μs (x = 0.02) to 1528.3 μs (x = 0.05), indicating a change in the overall excited-state relaxation dynamics with Dy^{3+} concentration. This trend is consistent with the photoluminescence intensity results, where x = 0.05 exhibits maximum emission, however it should not be interpreted as direct evidence of improved radiative efficiency without quantum efficiency or radiative-rate analysis. The absence of an abrupt decrease in lifetime beyond the optimal concentration, together with the previously calculated critical distance ($R_c \approx 8.8$ Å), supports a concentration quenching mechanism governed by long-range multipolar interactions rather than short-range exchange coupling. Upon alkali co-doping, a further modification of the decay dynamics is observed. According to Table 4, the YBBO:0.05Dy^{3+},0.02 K^{+} sample exhibits a significantly prolonged lifetime of 2117.4 μs, whereas the YBBO:0.05Dy^{3+},0.02Na^{+} sample shows a moderate increase to 1646.5 μs. This comparison indicates that a longer lifetime does not necessarily correspond to higher emission intensity.

The longer lifetime observed for the K^{+} co-doped sample may be related to alkali-induced modification of the local environment and overall relaxation dynamics. However, the present data do not allow a direct separation of radiative (k_r) and non-radiative (k_{nr}) relaxation processes. It should be noted that a longer decay lifetime does not necessarily imply a higher emission intensity. In principle, the average lifetime depends on the total excited-state depopulation rate, whereas the emission efficiency depends on the relative contributions of radiative and non-radiative processes. However, quantitative evaluation of these contributions requires absolute quantum efficiency and radiative/non-radiative rate analysis, which were not performed in the present work. Therefore, the longer lifetime of the K^{+} co-doped sample is interpreted as slower overall excited-state depopulation, whereas the stronger steady-state PL intensity of the Na^{+} co-doped sample indicates more favorable emission output under the present experimental conditions. In contrast, Na^{+} co-doping provides the strongest steady-state emission intensity together with millisecond-scale lifetime; however this should be regarded as a comparative observation rather than direct proof of optimized radiative efficiency. Furthermore, the multi-exponential decay behavior suggests a distribution of local environments around Dy^{3+} ions, which is influenced by alkali incorporation. This observation is consistent with the structural analysis, where Na^{+} co-doping produces less disruptive average lattice modification compared with K^{+}. Such a structural environment may contribute to the observed emission enhancement, although direct evidence for more efficient radiative recombination would require quantum efficiency or rate-constant analysis. The obtained lifetime values ($\tau_{avg} \approx$ 1.2–2.1 ms) fall within the typical range reported for Dy^{3+}-activated borate and oxide phosphors, supporting the suitability of the YBBO host for Dy^{3+}-based emission [2,80,97,98].

Overall, the lifetime analysis demonstrates that alkali co-doping modifies decay dynamics of Dy^{3+} ions, while changes in emission efficiency are inferred only qualitatively from the steady-state PL response. Among the studied compositions, Na^{+} co-doping gives the strongest steady-state PL enhancement together with a millisecond-scale lifetime, making it the most favorable composition within the present comparative study. However, a definitive assessment of radiative efficiency

requires absolute quantum yield and radiative/non-radiative rate measurements. This contrast between lifetime and emission intensity is discussed together with the emission-derived effective Judd–Ofelt-type analysis, which provides comparative information on relative emission redistribution. However, it should not be considered direct proof of radiative transition redistribution in the conventional Judd–Ofelt sense.

4.6. Judd–Ofelt analysis and radiative properties

It should be emphasized that the parameters denoted as $\Omega_{2,eff}$, $\Omega_{4,eff}$, and $\Omega_{6,eff}$ in this work are not absolute Judd–Ofelt intensity parameters obtained from absorption spectroscopy. Instead, they are emission-derived effective intensity parameters calculated from relative emission transition probabilities and are used here as empirical indicators of changes in the local crystal-field environment. Therefore, the obtained values should be interpreted qualitatively rather than as true Judd–Ofelt parameters.

In the present work, the Judd–Ofelt analysis is primarily utilized to elucidate how variations in effective intensity parameters reflect structural distortion and govern the observed emission behavior. The following discussion is therefore presented within a Judd–Ofelt-type framework and uses emission-derived effective intensity parameters rather than absolute Judd–Ofelt parameters. The J–O formalism provides a quantitative description of electric-dipole transitions of rare-earth ions through three phenomenological intensity parameters, Ω_2, Ω_4, and Ω_6. Among these parameters, Ω_2 is highly sensitive to the local asymmetry and covalency of the ligand environment, whereas Ω_4 and Ω_6 are associated with long-range crystal-field effects and lattice rigidity.

In a conventional Judd–Ofelt analysis, the experimental oscillator strength is obtained from absorption spectra using:

$$f_{exp} = 4.318 \times 10^{-9} \int \varepsilon(\nu) d\nu \tag{3}$$

where $\varepsilon(\nu)$ is the molar absorption coefficient and ν is the transition frequency.

The calculated oscillator strength is given by:

$$f_{cal} = \frac{8\pi^2 mc\upsilon}{3h(2J+1)} \cdot \frac{(n^2+2)^2}{9n} \sum_{\lambda=2,4,6} \Omega_\lambda \left| \langle \psi_J \left\| U^{(\lambda)} \right\| \psi'_J \rangle \right|^2 \tag{4}$$

The parameters in Eq. (4) have their usual physical meanings. Here, m denotes the electron rest mass, c is the speed of light in vacuum, and h represents Planck's constant. The term n corresponds to the refractive index of the host material, while (2 J + 1) indicates the degeneracy of the initial state. The quantity ν is the transition wavenumber expressed in cm^{-1}. The refractive index parameter is introduced as part of the standard Judd–Ofelt formalism; however, it was not directly involved in the present calculations due to the use of emission-derived relative oscillator strengths. The terms $\left| \langle \psi_J \left\| U^{(\lambda)} \right\| \psi'_J \rangle \right|^2$ are the doubly reduced matrix elements of the unit tensor operator, which are independent of the host environment [99]. The parameters Ω_λ (λ = 2,4,6) represent the Judd–Ofelt intensity parameters that characterize the strength of electric-dipole transitions and provide information about the local symmetry and bonding environment around the Dy^{3+} ions. These quantities are discussed here only to introduce the conventional Judd–Ofelt formalism and should not be confused with the emission-derived Ωλ,eff parameters used in the present work.

The Judd–Ofelt intensity parameters are typically obtained by minimizing the deviation between experimental and calculated oscillator strengths:

$$\sum \left(f_{exp} - f_{cal} \right)^2 \rightarrow min \tag{5}$$

In the present study, due to the absence of reliable absorption spectra for powder samples, an emission-based approach was adopted. This methodology is sometimes used when diffuse reflectance or absolute absorption data are not available and provides only a comparative evaluation of relative emission behavior. Accordingly, normalized integrated emission intensities were employed to estimate relative effective intensity parameters ($\Omega_{\lambda,eff}$) rather than absolute Judd–Ofelt intensity parameters derived from absorption oscillator strengths. It should be emphasized that the present Ωλ,eff values are not directly comparable, on a quantitative basis, with conventional absorption- or excitation-derived Judd–Ofelt intensity parameters reported in the literature. In rigorous Judd–Ofelt analyses, Ω_2, Ω_4, and Ω_6 are obtained by fitting experimental oscillator strengths and evaluating the deviation between measured and calculated values. In contrast, the present approach is based on normalized integrated emission contributions and is therefore used only to describe relative changes in the observed Dy^{3+} emission distribution. Accordingly, comparisons with previously reported Dy^{3+}-activated phosphors are made only at the qualitative level, focusing on general structure–luminescence trends rather than on absolute Ωλ values, oscillator strengths, radiative probabilities, or quantum efficiency.

The emission spectra exhibit three main transitions corresponding to $^4F_{9/2} \rightarrow {}^6H_{13/2}$ (576 nm), $^4F_{9/2} \rightarrow {}^6H_{11/2}$ (660 nm), and $^4F_{9/2} \rightarrow {}^6F_{11/2}/{}^6H_{9/2}$ (760 nm).

These transitions were selected based on their sufficiently resolved spectral profiles and their relevance to the observed Dy^{3+} emission distribution. Possible overlap effects were considered qualitatively, and the 760 nm band was treated as a combined transition due to spectral overlap. However, the present emission-based approach does not allow rigorous deconvolution of overlapping components or explicit separation of electric- and magnetic-dipole contributions. Although a larger number of transitions is generally preferred for a full Judd–Ofelt analysis, the present study utilizes the most prominent and well-resolved emission bands to provide a reliable comparative evaluation.

The relative oscillator strengths were estimated from integrated emission areas:

$$f_{rel} = \frac{A}{\lambda} \tag{6}$$

where A is the integrated emission intensity and λ is the emission wavelength.

The experimental branching ratios were calculated as:

$$\beta_{exp} = \frac{A_i}{\sum A_i} \tag{7}$$

where A_i is the integrated emission area of each transition. It should be noted that magnetic-dipole contributions were not explicitly separated in the present emission-based analysis. Therefore, the obtained Ωλ,eff values should not be interpreted as pure electric-dipole Judd–Ofelt parameters or as direct measures of radiative transition probabilities.

To interpret the results within the Judd–Ofelt framework, emission-derived effective intensity parameters were estimated as normalized contributions (Table 5):

$$\Omega_{\lambda,eff} = \frac{f_{rel,i}}{\sum f_{rel}} \tag{8}$$

It should be noted that these parameters represent normalized relative contributions derived from emission intensities and do not correspond to absolute Judd–Ofelt parameters obtained from absorption spectra. The emission bands at 576 nm, 660 nm, and 760 nm were used to estimate normalized effective intensity parameters ($\Omega_{\lambda,eff}$) based on their relative integrated emission contributions. However, these bands should not be regarded as pure or independent Ω_2, Ω_4, and Ω_6 contributions because of possible spectral overlap, mixed electric-/magnetic-dipole character, and the absence of explicit magnetic-dipole separation.

It should also be emphasized that the present emission-derived $\Omega_{\lambda,eff}$ parameters do not establish a direct physical correspondence between

Table 5
Integrated emission areas (A_i), relative oscillator strengths (f_{rel}), experimental branching ratios (β_{exp}), and emission-derived effective Judd–Ofelt parameters ($\Omega_{\lambda,eff}$) of YBBO:Dy^{3+} phosphors. The relative oscillator strengths were estimated using $f_{rel} = A_i/\lambda$. The reported $\Omega_{\lambda,eff}$ values represent normalized contributions derived from emission intensities and do not correspond to absolute Judd–Ofelt parameters obtained from absorption spectra.

Sample	Transition	λ (nm)	A_i(a.u.)	f_{rel} (a.u.)	β_{exp}	$\Omega_{\lambda,eff}$
YBBO:0.05Dy^{3+}	$^4F_{9/2} \rightarrow {}^6H_{13/2}$	576	1,964,493	3410.58	0.395	$\Omega_2 = 0.436$
	$^4F_{9/2} \rightarrow {}^6H_{11/2}$	660	2,266,977	3434.81	0.455	$\Omega_4 = 0.439$
	$^4F_{9/2} \rightarrow {}^6F_{11/2}/{}^6H_{9/2}$	760	747,004	982.90	0.150	$\Omega_6 = 0.126$
YBBO:0.05Dy^{3+},0.02Na^+	$^4F_{9/2} \rightarrow {}^6H_{13/2}$	576	2,389,537	4148.50	0.312	$\Omega_2 = 0.349$
	$^4F_{9/2} \rightarrow {}^6H_{11/2}$	660	4,153,081	6292.55	0.543	$\Omega_4 = 0.529$
	$^4F_{9/2} \rightarrow {}^6F_{11/2}/{}^6H_{9/2}$	760	1,110,731	1461.49	0.145	$\Omega_6 = 0.123$
YBBO:0.05Dy^{3+},0.02K^+	$^4F_{9/2} \rightarrow {}^6H_{13/2}$	576	1,168,590	2028.80	0.231	$\Omega_2 = 0.262$
	$^4F_{9/2} \rightarrow {}^6H_{11/2}$	660	3,022,482	4579.52	0.598	$\Omega_4 = 0.591$
	$^4F_{9/2} \rightarrow {}^6F_{11/2}/{}^6H_{9/2}$	760	863,754	1136.52	0.171	$\Omega_6 = 0.147$

an individual emission band and a single Judd–Ofelt $\Omega\lambda$ contribution. Possible spectral overlap, mixed electric-/magnetic-dipole character of the observed transitions, and the absence of explicit magnetic-dipole separation limit such a direct interpretation. Therefore, $\Omega_{2,eff}$, $\Omega_{4,eff}$, and $\Omega_{6,eff}$ are used here only as empirical comparative descriptors of relative emission changes among the observed Dy^{3+} bands. They should not be interpreted as absolute Judd–Ofelt intensity parameters, pure electric-dipole contributions, or direct radiative transition probabilities. A rigorous separation of these contributions would require conventional absorption-based Judd–Ofelt analysis, oscillator-strength fitting, spectral deconvolution, and explicit treatment of electric- and magnetic-dipole components.

The emission-derived effective Judd–Ofelt-typeparameters provide a comparative indication of how the relative Dy^{3+} emission contributions vary upon alkali co-doping. The increase in Ω_4,eff observed in the co-doped samples, particularly for K^+ incorporation, is consistent with the enhanced dominance of the 660 nm emission band and may be associated with structural perturbations inferred from XRD and size–-strain analyses. However, because these parameters are derived from emission intensities rather than absorption-based Judd–Ofelt fitting, and because direct local coordination information is not available, they should not be interpreted as definitive evidence of local symmetry changes. Instead, the observed variations in $\Omega_{\lambda,eff}$, branching ratios, PL intensity, and lifetime behavior provide comparative support for a possible relationship between alkali-induced structural modification and changes in the relative Dy^{3+} emission distribution.

The results indicate that the $^4F_{9/2} \rightarrow {}^6H_{11/2}$ transition at 660 nm is the dominant emission channel for all compositions. The branching ratio of this transition increases from 0.455 in the singly doped sample to 0.543 and 0.598 for Na^+ and K^+ co-doped samples, respectively.

The emission-derived effective intensity parameters ($\Omega_{\lambda,eff}$) indicate that alkali co-doping changes the relative emission contributions of the observed Dy^{3+} bands. The singly doped sample exhibits comparable $\Omega_{2,eff}$ (0.436) and $\Omega_{4,eff}$ (0.439) values, whereas co-doping leads to a pronounced increase in $\Omega_{4,eff}$, reaching a maximum value of 0.591 for the K^+ co-doped sample. This trend indicates an increased relative contribution of the 660 nm red emission band. Although this may be associated with changes in the Dy^{3+} local environment, the present emission-derived analysis cannot directly quantify crystal-field perturbation or electric-/magnetic-dipole contributions. However, it should be noted that the emission-derived $\Omega_{\lambda,eff}$ values represent relative contributions and do not allow a strict separation of local asymmetry and long-range crystal-field effects. This behavior is in agreement with the photoluminescence results, where the dominance of the 660 nm red emission band and the weaker contribution of shorter-wavelength emission components indicate an increased relative contribution of the red-emitting channel. The reduction of $\Omega_{2,eff}$ alongside the increase of $\Omega_{4,eff}$ suggests a change in the relative emission distribution; however, assigning this change to specific higher-rank crystal-field interactions requires conventional absorption-based Judd–Ofelt analysis.

Since the present analysis is based on emission-derived relative oscillator strengths rather than absorption-derived absolute values, a rigorous least-squares fitting procedure and RMS deviation could not be evaluated. Therefore, the $\Omega_{\lambda,eff}$ parameters should be interpreted as comparative indicators rather than absolute Judd–Ofelt parameters. Furthermore, the Na^+ co-doped sample exhibits the highest total emission intensity, while the K^+ co-doped sample shows the highest relative contribution of the 660 nm emission band. The increased branching ratio of the 660 nm transition indicates a stronger red-emission contribution, which influences the overall warm yellow–red color output. The observed behavior can be attributed to the modification of the local crystal-field environment. Alkali ions may introduce charge imbalance and lattice distortion, which can modify the local environment around Dy^{3+} ions; however, direct evidence for reduced local symmetry or enhanced parity mixing was not obtained in the present study. The stronger effect observed for K^+ is consistent with its larger ionic radius, leading to greater lattice distortion compared to Na^+. A comparison with previously reported Dy^{3+}-doped borate and tungstate hosts indicates that the observed Ω_4,eff-dominated trend is consistent with systems showing enhanced relative red-emission contribution under structural modification.

Consequently, quantities that strictly require absorption-derived oscillator strengths, including experimental oscillator strengths, integrated absorption areas, squared reduced matrix elements $\langle U(\lambda)\rangle^2$, and absolute radiative transition probabilities (A_{ed}, A_{md}, and AT), cannot be rigorously obtained from the present data set and are therefore beyond the scope of the present emission-derived analysis. The $\Omega_{\lambda,eff}$ values should thus be interpreted exclusively as comparative indicators of the relative emission contribution among the observed Dy^{3+} emission bands.

Overall, the emission-derived Judd–Ofelt-type analysis suggests that alkali co-doping modifies the relative Dy^{3+} emission distribution, providing a comparative framework for evaluating luminescence changes in YBBO-based phosphors. This behavior is qualitatively consistent with previously reported Dy^{3+}-activated phosphors, where changes in relative emission intensity, asymmetry ratio, and Judd–Ofelt-type parameters have been discussed in relation to host-structure effects, covalency, local symmetry, and lattice distortion. However, because the present $\Omega_{\lambda,eff}$ values are emission-derived comparative indicators, they are not directly compared numerically with conventional absorption- or excitation-derived Judd–Ofelt parameters reported in those studies [4, 26,100–102]. The results suggest that alkali co-doping influences luminescence behavior through possible lattice modification and changes in the relative emission distribution, linking structural and spectroscopic observations within a qualitative comparative framework. Therefore, the key outcome of the present emission-derived Judd–Ofelt-type analysis is not the determination of absolute Judd–Ofelt parameters, but the identification of a comparative trend: changes in Ω_4,eff are consistent with the dominance of the 660 nm red emission band and the associated changes in emission intensity and chromaticity behavior.

It should be emphasized that the present $\Omega_{\lambda,eff}$ values are derived

from normalized emission contributions and therefore do not represent absolute Judd–Ofelt intensity parameters obtained from conventional absorption-based oscillator-strength fitting. Consequently, these values cannot be used to directly determine parity mixing, electric-/magnetic-dipole separation, absolute radiative transition probabilities, or definitive crystal-field perturbation. The observed $\Omega_{4,eff}$ variation is therefore discussed only as a comparative indicator of the increased relative contribution of the 660 nm red emission band. Direct confirmation of the microscopic origin of this behavior would require conventional absorption-based Judd–Ofelt analysis, absolute quantum efficiency measurements, radiative/non-radiative rate analysis, and/or local-structure probes.

4.7. Chromaticity coordinates, correlated color temperature and color purity analysis

The colorimetric performance of YBBO:Dy^{3+} and alkali co-doped phosphors was systematically evaluated using the Commission Internationale de l'Éclairage (CIE) 1931 chromaticity diagram. The calculated chromaticity coordinates (x, y), correlated color temperature (CCT), and color purity (CP) values are summarized in Table 6, while their corresponding positions are illustrated in Fig. 9(a–c).

For the singly doped YBBO:$x$$Dy^{3+}$ system, the chromaticity coordinates are located in the yellowish–warm white region, with coordinates shifting slightly from (0.4574, 0.5248) to (0.3948, 0.5829) as the Dy^{3+} concentration increases from x = 0.005 to 0.07. This trend indicates a gradual movement within the warm-white/yellow region of the CIE diagram, governed by the relative contributions of the 576 nm yellow and 660 nm red emission bands. The corresponding CCT values vary between 3455 K and 4527 K, confirming that all compositions fall within the warm white to neutral white region, which is highly desirable for indoor lighting applications. The color purity increases from 57% to 64% with increasing Dy^{3+} content, reflecting enhanced relative contribution of the yellow (~576 nm) and red (~660 nm) emission bands. In particular, the strong $^4F_{9/2} \rightarrow {}^6H_{11/2}$ transition at ~660 nm contributes to the red component of the overall emission. Upon K^+ co-doping, a noticeable modification in chromaticity behavior is observed. The emission coordinates shift within a narrower region, approximately spanning x = 0.4131–0.4674 and y = 0.5076–0.5674. Compared to the singly doped system, the K^+ co-doped samples remain within the warm-white/yellow-red region, with chromaticity variations mainly governed by changes in the relative yellow and red emission contributions. The CCT values range between 3239 K and 4002 K, indicating a tendency toward warmer emission characteristics. However, the color purity remains relatively moderate (55–59%), suggesting that although K^+ co-doping enhances emission intensity it also modifies the relative spectral distribution. This behavior is consistent, in a comparative sense, with the stronger red contribution and the higher emission-derived $\Omega_{4,eff}$ trend discussed in Section 4.6.

In contrast, Na^+ co-doping results in a more balanced chromaticity distribution. The emission coordinates are located within x = 0.3991–0.4581 and y = 0.5258–0.5799, exhibiting a controlled shift toward the yellow region without significant deviation. Notably, the Na^+ co-doped sample at y = 0.03 displays coordinates (0.3991, 0.5799), indicating a comparatively balanced warm-white/yellow-red emission among the studied compositions. The corresponding CCT values span from 3467 K to 4457 K, indicating a stable warm-to-neutral white emission. Importantly, one of the highest color purity values (~64%) is achieved for this composition, highlighting the effectiveness of Na^+ co-doping in tuning the emission color quality.

The observed chromaticity shifts can be qualitatively associated with changes in the relative emission distribution, particularly the increased contribution of the 660 nm red band. As suggested by the emission-derived Judd–Ofelt-type analysis, the higher $\Omega_{4,eff}$ trend in the co-doped samples is consistent with an increased relative contribution of the 660 nm red emission band, resulting in a chromaticity shift toward the warm yellow–red region. This trend is more pronounced in the K^+ co-doped samples and is qualitatively consistent with their higher XRD-derived lattice distortion, whereas Na^+ co-doping maintains a more balanced relative emission distribution, leading to improved color purity and chromatic stability.

Furthermore, the obtained CCT values (~3200–4500 K) fall within the optimal range for warm white lighting applications, such as residential and display illumination. The moderate-to-high color purity values (up to ~64%) combined with tunable chromaticity coordinates indicate that the YBBO^{3+} system has potential for single-phase color tuning in warm-white/yellow-red emission applications. The observed decrease in CCT indicates a progressive shift of the emission toward the warm-white region. Consequently, a decrease in CCT is observed only when the relative spectral balance changes; a proportional increase or decrease of all emission bands would not alter the CCT value. It should be noted that CCT is not directly governed by the absolute emission intensity but rather by the normalized spectral distribution of the emitted light. Therefore, changes in the relative contributions of the blue-region host-/defect-related feature, the Dy^{3+} yellow band at ~576 nm, and the Dy^{3+} red band at ~660 nm can significantly influence the chromaticity coordinates and consequently the CCT values. In the present system, the reduction in CCT suggests an increased contribution of the longer-wavelength emission components relative to the shorter-wavelength region, resulting in a warmer emission appearance. Similar CCT reductions associated with enhanced yellow/red emission have been reported in Dy^{3+}- and rare-earth-co-doped phosphors, where energy-transfer processes and local crystal-field modifications alter the spectral balance and shift the chromaticity coordinates toward the warm-white region [103–105]. Therefore, the observed CCT variation in the present phosphors is primarily related to changes in the relative emission-band intensities rather than the overall luminescence intensity.

Overall, the chromaticity results indicate that Dy^{3+} concentration and alkali co-doping modify the relative spectral distribution of the YBBO:Dy^{3+} phosphors, leading to systematic changes in CIE coordinates, CCT, and color purity. These variations are primarily associated with changes in the relative contributions of the 576 nm yellow and 660 nm red emission bands. In particular, the increased contribution of

Table 6
CIE 1931 chromaticity coordinates (x, y), correlated color temperature (CCT), and color purity (CP%) of YBBO:$x$$Dy^{3+}$, YBBO:0.05$Dy^{3+}$,$y$$K^+$, and YBBO:0.05$Dy^{3+}$,$y$$Na^+$ phosphors under 370 nm excitation. The data demonstrate the effect of Dy^{3+} concentration and alkali co-doping on emission color tuning, revealing systematic variations in chromaticity coordinates, warm-white CCT range, and color purity, with Na^+ co-doping providing the most balanced color characteristics.

Dy^{3+} content (wt.%)	x	y	CCT	Color Purity (CP)%
0.5	0.4574	0.5248	3455	57
1	0.4138	0.5671	4213	62
2	0.4188	0.5618	4126	61
3	0.4422	0.5461	3749	60
5	0.4131	0.5674	4223	62
7	0.3948	0.5829	4527	64
K^+ content (wt.%)	***x***	***y***	**CCT**	**Color Purity (CP)%**
0.5	0.4254	0.5525	4002	59
1	0.4674	0.5076	3239	55
2	0.4529	0.5290	3533	57
3	0.4230	0.5410	3995	56
5	0.4288	0.5365	3895	56
7	0.4297	0.5354	3877	56
Na^+ content (wt.%)	***x***	***y***	**CCT**	**Color Purity (CP)%**
0.5	0.4417	0.5380	3722	58
1	0.4390	0.5292	3722	55
2	0.4430	0.5258	3652	55
3	0.3991	0.5799	4457	64
5	0.4463	0.5368	3655	58
7	0.4581	0.5293	3467	58

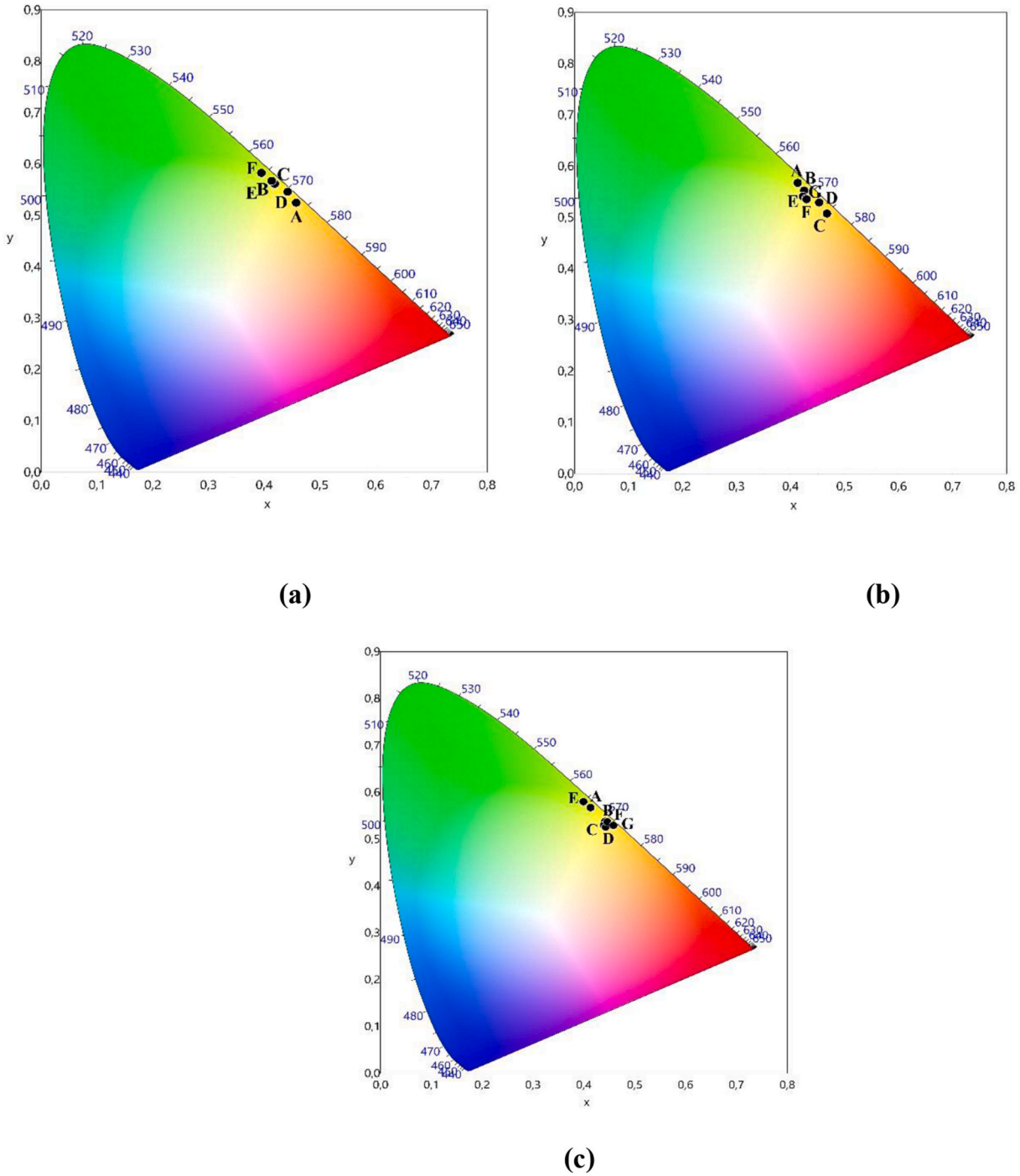

Fig. 9. CIE 1931 chromaticity diagrams of (a) YBBO:xDy^{3+} (x = 0.005–0.07), (b) YBBO:0.05Dy^{3+},yK^{+} (y = 0–0.07), and (c) YBBO:0.05Dy^{3+},yNa^{+} (y = 0–0.07) phosphors under 370 nm excitation.

the 660 nm red emission band shifts the chromaticity toward the warm yellow–red region. However, this color evolution should be regarded as a comparative spectroscopic trend rather than direct proof of a causal relationship between lattice distortion, $\Omega_{4,\mathrm{eff}}$ variation, and radiative transition redistribution. The colorimetric analysis is therefore discussed in terms of the measured PL spectral distribution, while the proposed structure–property relationship remains indirect and qualitative.

5. Conclusion

Dy^{3+}-activated $YBa_3B_9O_{18}$ phosphors co-doped with Na^{+} and K^{+} ions were successfully synthesized, and their structural, photoluminescence, decay, thermal-quenching, and colorimetric properties were systematically investigated. Structural analyses confirmed the formation of a single-phase hexagonal YBBO structure for all compositions. XRD-derived crystallite-size and microstrain results indicated that alkali incorporation modifies the average lattice structure, with K^{+} producing relatively higher lattice distortion and Na^{+} maintaining a comparatively less disrupted framework.

Under near-UV excitation, the phosphors exhibited characteristic Dy^{3+} emissions at ~576 nm, ~660 nm, and ~760 nm, corresponding to yellow, red, and deep-red emission components, respectively. The optimum Dy^{3+} concentration was x = 0.05, and concentration quenching was mainly associated with long-range multipolar interactions. Alkali

co-doping enhanced the emission intensity, with Na^+ providing the strongest PL enhancement, while K^+ increased the relative contribution of the 660 nm red emission band.

The emission-derived $\Omega_{\lambda,eff}$ parameters were used only as comparative indicators of relative emission redistribution and not as absolute Judd–Ofelt intensity parameters. Within this framework, the observed Ω_4,eff trend was consistent with the increased relative contribution of the 660 nm red band. Temperature-dependent PL measurements showed that alkali co-doping improved the high-temperature PL retention compared with the singly doped phosphor, although the proposed relationship between lattice modification and thermal stability remains indirect and literature-supported. Lifetime analysis further indicated that alkali incorporation modifies the overall Dy^{3+} excited-state relaxation dynamics, without allowing direct separation of radiative and non-radiative rates.

CIE analysis confirmed tunable warm-white to yellow-red emission, mainly governed by the relative balance between the 576 nm yellow and 660 nm red bands. Overall, the present results indicate that Na^+/K^+ co-doping provides a useful route for tuning the luminescence response of $YBBO^{3+}$ phosphors. However, further absolute quantum efficiency, conventional absorption-based Judd–Ofelt analysis, and device-level investigations are required to fully evaluate their practical applicability in pc-WLEDs.

CRediT authorship contribution statement

O. Madkhali: Formal analysis, Investigation, Methodology. **Jabir Hakami:** Formal analysis, Investigation, Methodology. **H. Aydin:** Investigation, Methodology, Software. **Ş. Demiç:** Conceptualization, Investigation. **M. Can:** Data curation, Investigation. **U.H. Kaynar:** Formal analysis, Investigation, Methodology, Resources, Software. **M.B. Coban:** Investigation, Methodology, Software. **N. Can:** Funding acquisition, Investigation, Methodology, Project administration, Supervision, Writing – original draft, Writing – review & editing.

Declaration of competing interest

The authors declare that they have no known competing financial interests or personal relationships that could have appeared to influence the work reported in this paper.

Acknowledgement

The authors would like to express their sincere gratitude to the Research Fund of Balikesir University (Grant No. BAP-2026/019) for financial support.

Data availability

Data will be made available on request.

References

[1] D. Gao, Y. Li, L. Cheng, S. Liu, S. Xu, X. Li, J. Zhang, X. Zhang, Y. Cao, Y. Wang, X. Wang, Y. Zhang, X. Sha, L. Wang, B. Chen, Concentration effects of fluorescence quenching and optical transition properties of Dy^{3+} doped NaYF4 phosphor, J. Alloys Compd. 895 (2022) 162616, https://doi.org/10.1016/j.jallcom.2021.162616.

[2] K. Poria, R. Lohan, S. Bhatia, A. Kumar, R. Singh, N. Deopa, R. Punia, J.S. Shahi, A.S. Rao, Lumino-structural properties of Dy^{3+} activated $Na_3Ba_2LaNb_{10}O_{30}$ phosphors with enhanced internal quantum yield for w-LEDs, RSC Adv. 13 (2023) 11557–11568, https://doi.org/10.1039/D3RA01260C.

[3] M.B. Coban, J. Hakami, H. Aydin, U.H. Kaynar, E. Aymila Çin, T. Karaman, M. Sharahili, O. Madkhali, D. Somaily, R. Karmouch, N. Can, Structural and luminescence properties of alkali-co-doped $LiCaBO_3$:Dy^{3+} phosphors, Appl. Radiat. Isot. 227 (2026) 112288, https://doi.org/10.1016/j.apradiso.2025.112288.

[4] V. Rathina Mala, P. Balakrishnan, S. Masilla Moses Kennedy, Effect of co-doping alkali metal ions $Li^+/Na^+/K^+$ on the photoluminescence enhancement properties of the near white light emitting $LiSrVO_4$:Dy^{3+} phosphor along with the optical transition probabilities by Judd-Ofelt analysis for WLEDs application, Solid State Sci. 138 (2023) 107131, https://doi.org/10.1016/j.solidstatesciences.2023.107131.

[5] R. Zhao, X. Guo, J. Zhang, C. Zhang, C. Deng, R. Cui, Thermally-stable novel $NaBaBi_2(PO_4)_3$: Sm^{3+}/Dy^{3+} white phosphors with tunable photoluminescence, Ceram. Int. 49 (2023) 25795–25805, https://doi.org/10.1016/j.ceramint.2023.05.126.

[6] J. Dahiya, A. Hooda, A. Agarwal, S. Khasa, Detailed optical analysis of Dy^{3+} and Pr^{3+} co-doped alumino-borate glasses for visible lighting applications, Ceram. Int. 49 (2023) 15284–15294, https://doi.org/10.1016/j.ceramint.2023.01.112.

[7] J. Dahiya, A. Sharma, A. Hooda, M. Malik, A. Khatri, S. Khasa, Influence of different alkali fluorides (LiF/NaF/KF) on photoluminescence properties of Dy^{3+} and Eu^{3+} rare Earth ion Co-Doped borate glasses, J. Electron. Mater. 53 (2024) 7495–7508, https://doi.org/10.1007/s11664-024-11435-9.

[8] U.H. Kaynar, H. Aydin, A.S. Altowyan, J. Hakami, M.B. Coban, M. Ayvacikli, E. Ekdal Karali, A. Canimoglu, N. Can, Enhancement of luminescence and thermal stability in Eu^{3+}-doped $K_3Y(BO_2)_6$ with Li^+ and Na^+ co-doping, Adv. Powder Technol. 35 (2024) 104695, https://doi.org/10.1016/j.apt.2024.104695.

[9] A.K. Kunti, N. Patra, S.K. Sharma, H.C. Swart, Radiative transition probability enhancement of white light emitting Dy^{3+} doped and K^+ co-doped $BaWO_4$ phosphors via charge compensation, J. Alloys Compd. 735 (2018) 2410–2422, https://doi.org/10.1016/j.jallcom.2017.11.357.

[10] B. Abidine, M. Yahya, M. Mhadhbi, C. Bouzidi, A.H. Hamzaoui, Characterization and luminescence properties of Eu^{3+} doped $BaCO_3$ nanoparticles synthesized by autocombustion method, J. Mol. Struct. 1263 (2022) 133122, https://doi.org/10.1016/j.molstruc.2022.133122.

[11] A. Abdallah, C. Bouzidi, Optical studies of Dy_2O_3 doped phosphate glasses for potential white luminescence applications, Solid State Sci. 165 (2025) 107958, https://doi.org/10.1016/j.solidstatesciences.2025.107958.

[12] R. Divina, P.E. Teresa, K. Marimuthu, Dy^{3+} ion as optical probe to study the luminescence behavior of alkali lead bismuth borate glasses for w-LED application, J. Alloys Compd. 883 (2021) 160845, https://doi.org/10.1016/j.jallcom.2021.160845.

[13] M. Behera, R. Panda, R. Arun Kumar, N.K. Mishra, K. Kumar, T. Del Monte, Microwave-assisted combustion synthesis and characterization studies of novel dysprosium doped yttrium calcium borate (Dy^{3+}:$Y_2CaB_{10}O_{19}$) phosphor materials for efficient white light applications, Ceram. Int. 50 (2024) 18146–18156, https://doi.org/10.1016/j.ceramint.2024.02.298.

[14] P. Deepa, P. Murugasen, A.A. Suresh, M. Dhavamurthy, A.V. Deepa, Luminescence features of Dy^{3+}-doped B_2O_3 and B_2O_3-P_2O_5 hosts for optical devices: the linear and non-linear optical studies, Emerg. Mater. 7 (2024) 1715–1731, https://doi.org/10.1007/s42247-024-00696-z.

[15] V. Anthony Raj, K. Maheshvaran, K. Marimuthu, I. Arul Rayappan, Structural and luminescence properties of Dy^{3+}-doped alkali fluoroborophosphate glasses for white LEDs applications, Indian J. Phys. 94 (2020) 1395–1407, https://doi.org/10.1007/s12648-019-01587-4.

[16] N. Baig, R.S. Yadav, N.S. Dhoble, V.L. Barai, S.J. Dhoble, Near UV excited multi-color photoluminescence in RE^{3+} (RE=Tb, Sm, Dy and Eu) doped $Ca_2Pb_3(PO_4)_3Cl$ phosphors, J. Lumin. 215 (2019) 116645, https://doi.org/10.1016/j.jlumin.2019.116645.

[17] I. Ayoub, V. Kumar, Synthesis, photoluminescence, Judd–Ofelt analysis, and thermal stability studies of Dy^{3+} -doped $BaLa_2ZnO_5$ phosphors for solid-state lighting applications, RSC Adv. 13 (2023) 13423–13437, https://doi.org/10.1039/D3RA02659K.

[18] P.N.K. Chaitanya, D. Haranath, D. Dinakar, M.S. Ramana, K.V.R. Murthy, M. Rakshita, G. Gupta, Structural and luminescent properties of Dy^{3+}-doped Ca_3WO_6 phosphors for white-light display applications, RSC Adv. 15 (2025) 19872–19883, https://doi.org/10.1039/D5RA02648B.

[19] A. Douzi, S. Slimi, E. Madirov, A. Turshatov, B.S. Richards, R.M. Solé, M. Aguiló, F. Díaz, E. Ben Salem, X. Mateos, Structure and luminescence properties of Dy^{3+} doped quaternary tungstate $Li_3Ba_2Gd_3(WO_4)_8$ for application in wLEDs, RSC Adv. 13 (2023) 23772–23787, https://doi.org/10.1039/D3RA02501B.

[20] F. Xie, J. Gu, D. Xu, H. Lin, Y. Shi, S. Zhang, D. Wang, R. Zhu, J. Yang, Tunable emission color, energy transfer mechanisms and high thermal stability of Tm^{3+}/Dy^{3+} co-doped single-phase white luminescent tungstate phosphors, J. Lumin. 269 (2024) 120519, https://doi.org/10.1016/j.jlumin.2024.120519.

[21] R. Chen, X. Jiang, T. Zhang, F. Zeng, W. Yang, H. Lin, L. Liu, S. Li, C. Li, Z. Su, A white-emitting $CaY_2Al_4SiO_{12}$: Dy^{3+} phosphors with excellent optical properties and thermal stability by partially substituting Y^{3+} with Gd^{3+}, J. Alloys Compd. 966 (2023) 171558 https://doi.org/10.1016/j.jallcom.2023.171558.

[22] X. Huang, W. Zhang, X. Wang, J. Zhang, Optical characteristics and energy transfer between Eu^{3+} and Dy^{3+} in Na_2CaSiO_4:Dy^{3+}, Eu^{3+} white-emitting phosphor, J. Alloys Compd. 873 (2021) 159803, https://doi.org/10.1016/j.jallcom.2021.159803.

[23] B.S. Kumar, H. Umamahesvari, K. Thyagarajan, P. Ankoji, V. Vijayakanth, Structural and photoluminescence properties of Dy^{3+}-doped $KMgBO_3$ phosphors, J. Mater. Sci. Mater. Electron. 34 (2023) 637, https://doi.org/10.1007/s10854-023-09974-8.

[24] S. Kumari Anu, N. Deopa, A.S. Rao, Spectral studies of thermally stable Dy^{3+}/Sm^{3+} co-doped $Li_2Ba_5W_3O_{15}$ phosphors for warm white LEDs, J. Phys. D Appl. Phys. 57 (2024) 315107, https://doi.org/10.1088/1361-6463/ad4566.

[25] J. Gu, F. Xie, S. Wang, D. Xu, H. Zhang, H. Xu, S. Zhong, Dy^{3+}/Tm^{3+} activated single-phase tungstate phosphors with anti-thermal quenching and tunable luminescence properties for white LEDs applications, Ceram. Int. 50 (2024) 14127–14138, https://doi.org/10.1016/j.ceramint.2024.01.318.

[26] C. Sonali, Shivakumara, enhanced emission intensity in (Li^+/Ca^{2+}/Bi^{3+}) ions co-doped $NaLa(MoO_4)_2$:Dy^{3+} phosphors and their Judd-Ofelt analysis for WLEDs applications, Methods Appl. Fluoresc. 11 (2023) 024001, https://doi.org/10.1088/2050-6120/acbbb9.

[27] N. Hussain, S. Rubab, V. Kumar, Spectroscopic characterizations and investigation of Judd-Ofelt intensity parameters of Dy^{3+}-doped $Ba_2La_8(SiO_4)_6O_2$ near white light emitting phosphor, Ceram. Int. 49 (2023) 15341–15348, https://doi.org/10.1016/j.ceramint.2023.01.118.

[28] A.S. Altowyan, U.H. Kaynar, H. Aydin, J. Hakami, M.B. Coban, K. Cikrikci, M. Ayvacikli, N. Can, Synthesis, structural characterization, and photoluminescence properties of Dy^{3+}-Doped CaB4O7 phosphors: influence of Li^+ and K^+ Co-doping, Mater. Sci. Semicond. Process. 195 (2025) 109593, https://doi.org/10.1016/j.mssp.2025.109593.

[29] F. Zhang, T. Zhang, G. Li, W. Zhang, Single phase M^+ (M = Li, Na, K), Dy^{3+} co-doped $KSrBP_2O_8$ white light emitting phosphors, J. Alloys Compd. 618 (2015) 484–487, https://doi.org/10.1016/j.jallcom.2014.08.178.

[30] Z. Li, X. Geng, Y. Wang, Y. Chen, Synthesis and luminescence properties of $NaBaPO_4$:Tm^{3+},Dy^{3+} white-light emitting phosphors with enhanced brightness by Li^+ co-doping, J. Lumin. 240 (2021) 118428, https://doi.org/10.1016/j.jlumin.2021.118428.

[31] R.S. Yadav, Monika, E. Rai, L.P. Purohit, S.B. Rai, Realizing enhanced downconversion photoluminescence and high color purity in Dy^{3+} doped $MgTiO_3$ phosphor in presence of Li^+ ion, J. Lumin. 217 (2020) 116810, https://doi.org/10.1016/j.jlumin.2019.116810.

[32] K. Wu, P. Xia, C. Ni, W. Li, M. Xu, W. Dai, High-Luminance red $Ba_2CaB_2Si_4O_{14}$:Eu^{3+} with "Abnormal" Thermal Stability and Adjustable Photoluminescence from Defect Regulation and Energy Transfer via Dy^{3+} Codoping for "Warm" illumination and pressure sensing applications, Cryst. Growth Des. 25 (2025) 3800–3812, https://doi.org/10.1021/acs.cgd.5c00232.

[33] P. Xia, Y. Lei, W. Li, K. Wu, C. Ni, M. Xu, W. Dai, Insight into tendentious multisite colonization, site environment modulation, and energy transfer of steady $Ba_2CaB_2Si_4O_{14}$:Ce/Tb/Sm/Sr/Na toward nUV-Pumped wLED application, Cryst. Growth Des. 24 (2024) 8031–8043, https://doi.org/10.1021/acs.cgd.4c00931.

[34] S.A. Khan, A. Jalil, Q. Ullah Khan, R.M. Irfan, I. Mehmood, K. Khan, M. Kiani, B. Dong, N.Z. Khan, J.-L. Yu, L. Zhu, S. Agathopoulos, New physical insight into crystal structure, luminescence and optical properties of YPO_4:Dy^{3+}\$Eu^{3+}$\$Tb^{3+}$ single-phase white-light-emitting phosphors, J. Alloys Compd. 817 (2020) 152687, https://doi.org/10.1016/j.jallcom.2019.152687.

[35] S.K. Sen, U.C. Barman, M.S. Manir, P. Mondal, S. Dutta, M. Paul, M.A. M. Chowdhury, M.A. Hakim, X-ray peak profile analysis of pure and Dy-doped α-MoO_3 nanobelts using Debye-Scherrer, Williamson-Hall and Halder-Wagner methods, Adv. Nat. Sci. Nanosci. Nanotechnol. 11 (2020) 025004, https://doi.org/10.1088/2043-6254/ab8732.

[36] A.S. Abdel-Rahman, Y.A. Sabry, An approach to the micro-strain distribution inside nanoparticle structure, Int. J. Non Lin. Mech. 161 (2024) 104670, https://doi.org/10.1016/j.ijnonlinmec.2024.104670.

[37] S. Mustapha, M.M. Ndamitso, A.S. Abdulkareem, J.O. Tijani, D.T. Shuaib, A. K. Mohammed, A. Sumaila, Comparative study of crystallite size using Williamson-Hall and Debye-Scherrer plots for ZnO nanoparticles, Adv. Nat. Sci. Nanosci. Nanotechnol. 10 (2019) 045013, https://doi.org/10.1088/2043-6254/ab52f7.

[38] M. Basak, M.L. Rahman, M.F. Ahmed, B. Biswas, N. Sharmin, The use of X-ray diffraction peak profile analysis to determine the structural parameters of cobalt ferrite nanoparticles using Debye-Scherrer, Williamson-Hall, Halder-Wagner and Size-strain plot: different precipitating agent approach, J. Alloys Compd. 895 (2022) 162694, https://doi.org/10.1016/j.jallcom.2021.162694.

[39] M. İlhan, M.K. Ekmekçi, L.F. Güleryüz, Effect of boron incorporation on the structural, morphological, and spectral properties of $CdNb_2O_6$:Dy^{3+} phosphor synthesized by molten salt process, Mater. Sci. Eng. B 298 (2023) 116858, https://doi.org/10.1016/j.mseb.2023.116858.

[40] M. İlhan, L.F. Güleryüz, M.İ. Katı, Exploring the effect of boron on the grain morphology change and spectral properties of Eu^{3+} activated barium tantalate phosphor, RSC Adv. 14 (2024) 2687–2696, https://doi.org/10.1039/D3RA08197D.

[41] M. İlhan, L.F. Güleryüz, A study on the structural, morphological, spectral properties of $BaTa_2O_6$:RE^{3+}, B^{3+} (RE = Sm, Dy) phosphors and the comparison of asymmetry ratios based on the hypersensitive transition of $BaTa_2O_6$:Eu^{3+}, B^{3+} phosphor, J. Mater. Sci. Mater. Electron. 36 (2025) 71, https://doi.org/10.1007/s10854-024-14139-2.

[42] M.M. El-shabaan, A. Mohamed, M.I. Youssif, N.A. El-Ghamaz, E.M. Ahmed, Comparative study on the influence of rare Earth ion doping on the structural and optical properties of simple B_2O_3–Na_2O glasses, Sci. Rep. 15 (2025) 35022, https://doi.org/10.1038/s41598-025-21224-x.

[43] M.A. Morsy, T.F. Garrison, M.R. Kessler, M.H.A. Mhareb, H.Z. El-Deen, Structural elucidation of lithium borate glasses using XRD, FTIR, and EPR spectroscopy, ACS Phys. Chem. Au 5 (2025) 227–238, https://doi.org/10.1021/acsphyschemau.4c00106.

[44] R. Bisi Deepali, Vandana, H. Kaur, M. Jayasimhadri, Structural and spectroscopic properties of Sm^{3+}-doped $NaBaB_9O_{15}$ phosphor for optoelectronic device applications, J. Mater. Sci. Mater. Electron. 32 (2021) 1650–1658, https://doi.org/10.1007/s10854-020-04934-y.

[45] Z. Tang, F. Du, H. Liu, Z. Leng, X. Sun, H. Xie, M. Que, Y. Wang, Eu^{2+} -doped layered double borate phosphor with ultrawide near-infrared spectral distribution in response to ultraviolet–blue light excitation, Adv. Opt. Mater. 10 (2022), https://doi.org/10.1002/adom.202102204.

[46] O. Madkhali, Ü.H. Kaynar, Y. Alajlani, M.B. Coban, J.G. Guinea, M. Ayvacikli, J. F. Pierson, N. Can, Structural and temperature dependence luminescence characteristics of RE (RE=Eu^{3+}, Dy^{3+}, Sm^{3+} and Tb^{3+}) in the new gadolinium aluminate borate phosphor, Ceram. Int. 49 (2023) 19982–19995, https://doi.org/10.1016/j.ceramint.2023.03.120.

[47] M. Peddaiah, C. Salma, B.H. Rudramadevi, Structural and an orange-red emission studies of Sm^{3+} doped $Ba_3La_2(BO_3)_4$ phosphor for solid state lighting application, Optik 244 (2021) 166695, https://doi.org/10.1016/j.ijleo.2021.166695.

[48] M. Manhas, V. Kumar, V.K. Singh, J. Sharma, R. Prakash, V. Sharma, A.K. Bedyal, H.C. Swart, A novel orange-red emitting $Ba_2Ca(BO_3)_2$:Sm^{3+} phosphor to fill the amber gap in LEDs: synthesis, structural and luminescence characterizations, Curr. Appl. Phys. 17 (2017) 1369–1375, https://doi.org/10.1016/j.cap.2017.07.015.

[49] K. Hristova, I.P. Kostova, T.A. Eftimov, G. Patronov, S. Tsoneva, Synthesis and characterization of smartphone-readable luminescent lanthanum borates doped and Co-Doped with Eu and Dy, Photonics 12 (2025) 171, https://doi.org/10.3390/photonics12020171.

[50] K.N. Boldyrev, B.N. Mavrin, M.N. Popova, L.N. Bezmaternykh, Spectroscopy of phonon and vibronic states of $YbAl_3(BO_3)_4$ single crystal, Opt. Spectrosc. 111 (2011) 420–425, https://doi.org/10.1134/S0030400X11090049.

[51] G.-W. Lu, C.-X. Li, W.-C. Wang, Z.-H. Wang, H.-R. Xia, H.-J. Zhang, X.-L. Meng, L.-X. Li, Lattice vibration and absorbance of Er:Yb:YCOB single crystals, Chem. Phys. Lett. 368 (2003) 269–275, https://doi.org/10.1016/S0009-2614(02)01855-9.

[52] R. Kaindl, G. Sohr, H. Huppertz, Experimental determinations and quantum-chemical calculations of the vibrational spectra of β-ZnB_4O_7 and β-CaB_4O_7, Spectrochim. Acta Part A Mol. Biomol. Spectrosc. 116 (2013) 408–417, https://doi.org/10.1016/j.saa.2013.07.072.

[53] V. Atuchin, A. Subanakov, A. Aleksandrovsky, B. Bazarov, J. Bazarova, A. Krylov, M. Molokeev, A. Oreshonkov, A. Pugachev, New double nonlinear-optical borate $Rb_3SmB_6O_{12}$: synthesis, structure and spectroscopic properties, J. Alloys Compd. 905 (2022) 164022, https://doi.org/10.1016/j.jallcom.2022.164022.

[54] G. Lakshminarayana, S.O. Baki, A. Lira, I.V. Kityk, U. Caldiño, K.M. Kaky, M. A. Mahdi, Structural, thermal and optical investigations of Dy^{3+}-doped B_2O_3–WO_3–ZnO–Li_2O–Na_2O glasses for warm white light emitting applications, J. Lumin. 186 (2017) 283–300, https://doi.org/10.1016/j.jlumin.2017.02.049.

[55] S.V. Demina, A.P. Shablinskii, A.V. Povolotskiy, R.S. Bubnova, Y.P. Biryukov, V. A. Firsova, S.K. Filatov, Synthesis, crystal structure, photoluminescence of $Ba_3Y_2(BO_3)_4$:Er^{3+} and thermal expansion of $Ba_3Y_2(BO_3)_4$, Ceram. Int. 49 (2023) 6459–6469, https://doi.org/10.1016/j.ceramint.2022.10.184.

[56] S. Guene-Girard, J. Courtois, M. Dussauze, J.-M. Heintz, A. Fargues, J. Roger, M. Nalin, T. Cardinal, V. Jubera, Comparison of structural and spectroscopic properties of Ho^{3+}-doped niobate compounds, Mater. Res. Bull. 143 (2021) 111451, https://doi.org/10.1016/j.materresbull.2021.111451.

[57] I. Gupta, D. Singh, P. Kumar, S. Singh, S. Bhagwan, V. Kumar, Structural, morphological, and optical characteristics of $Gd_2Si_2O_7$:Dy^{3+} nanophosphors for WLEDs, Luminescence 38 (2023) 1789–1802, https://doi.org/10.1002/bio.4566.

[58] P. Dewangan, D.P. Bisen, N. Brahme, S. Sharma, Structural characterization and luminescence properties of Dy^{3+} doped $Ca_3MgSi_2O_8$ phosphors, J. Alloys Compd. 777 (2019) 423–433, https://doi.org/10.1016/j.jallcom.2018.10.390.

[59] R. Yu, D.S. Shin, K. Jang, Y. Guo, H.M. Noh, B.K. Moon, B.C. Choi, J.H. Jeong, S. S. Yi, Photoluminescence properties of novel host-sensitized Y_6WO_{12}:Dy^{3+} phosphors, J. Am. Ceram. Soc. 97 (2014) 2170–2176, https://doi.org/10.1111/jace.12937.

[60] L. Reddy, A review of the efficiency of white light (or other) emissions in singly and Co-Doped Dy^{3+} ions in different host (Phosphate, Silicate, aluminate) materials, J. Fluoresc. 33 (2023) 2181–2192, https://doi.org/10.1007/s10895-023-03250-y.

[61] K. Griebenow, M.-P. Truong, F. Munoz, R. Klement, D. Galusek, Tuning the fluorescence of Dy^{3+} via the structure of borophosphate glasses, Sci. Rep. 13 (2023) 1919, https://doi.org/10.1038/s41598-023-28941-1.

[62] A. Douzi, S. Slimi, E. Madirov, J.M. Serres, R.M. Solé, E. Ben Salem, A. Turshatov, B.S. Richards, X. Mateos, Investigation of luminescence properties and ratiometric thermometry through yellow-to-blue Dy^{3+} emission in $Ca_3La_7(SiO_4)_5(PO_4)O_2$ apatite, RSC Adv. 15 (2025) 19623–19639, https://doi.org/10.1039/D5RA01912E.

[63] B. Han, B. Liu, Y. Dai, J. Zhang, Defect-induced luminescence of a self-activated borophosphate phosphor, J. Electron. Mater. 47 (2018) 4550–4554, https://doi.org/10.1007/s11664-018-6329-z.

[64] N. Krutyak, V. Nagirnyi, I. Romet, D. Deyneko, D. Spassky, Energy transfer processes in NASICON-type phosphates under synchrotron radiation excitation, Symmetry 15 (2023) 749, https://doi.org/10.3390/sym15030749.

[65] Z. Yang, S. Lai, Z. Xia, Self-activated luminescence in $AZn_4(BO_3)_3$ (A = K, Rb, Cs) and oxygen-defects-related photoluminescence tuning, J. Solid State Chem. 288 (2020) 121408, https://doi.org/10.1016/j.jssc.2020.121408.

[66] G.R. Dillip, G.B. Kumar, V.R. Bandi, M. Hareesh, B. Deva Prasad Raju, S.W. Joo, L. K. Bharat, J.S. Yu, Versatile host-sensitized white light emission in a single-component $K_3ZnB_5O_{10}$:Dy^{3+} phosphor for ultraviolet converted light-emitting diodes, J. Alloys Compd. 699 (2017) 1108–1117, https://doi.org/10.1016/j.jallcom.2017.01.008.

[67] Y. Chen, Y. Gao, R. Cong, T. Yang, Host-sensitized borate phosphors $ZnGdB_5O_{10}$:Mn^{2+}/Dy^{3+}/Sm^{3+}, Dalton Trans. 53 (2024) 17313–17323, https://doi.org/10.1039/D4DT02638A.

[68] A. Gu, G.-H. Pan, H. Wu, L. Zhang, L. Zhang, H. Wu, J. Zhang, Microstructure and photoluminescence of $ZrTiO_4$:Eu^{3+} phosphors: Host-Sensitized energy transfer and optical thermometry, Chemosensors 10 (2022) 527, https://doi.org/10.3390/chemosensors10120527.

[69] G.S. Ofelt, Intensities of crystal spectra of rare-earth ions, J. Chem. Phys. 37 (1962) 511–520, https://doi.org/10.1063/1.1701366.

[70] R.P. Leavitt, C.A. Morrison, Crystal-field analysis of triply ionized rare Earth ions in lanthanum trifluoride. II. Intensity calculations, J. Chem. Phys. 73 (1980) 749–757, https://doi.org/10.1063/1.440180.

[71] C. Görller-Walrand, L. Fluyt, A. Ceulemans, W.T. Carnall, Magnetic dipole transitions as standards for Judd–Ofelt parametrization in lanthanide spectra, J. Chem. Phys. 95 (1991) 3099–3106, https://doi.org/10.1063/1.460867.

[72] L. Huang, J. Qian, S. Sun, D. Li, Fixed Yellow-to-Blue intensity ratio of Dy^{3+} in KY$(CO_3)_2$ host for emission color tuning, Materials 17 (2024) 1438, https://doi.org/10.3390/ma17061438.

[73] D.J. Robbins, B. Cockayne, B. Lent, J.L. Glasper, The relationship between concentration and efficiency in rare Earth activated phosphors, J. Electrochem. Soc. 126 (1979) 1556–1563, https://doi.org/10.1149/1.2129329.

[74] U. Mushtaq, V. Kumar, Host-sensitized colour-tunable emission and Judd-ofelt analysis for Dy^{3+}-doped $ZnGa_2O_4$ phosphor through exciton-mediated energy transfer, Opt. Mater. 146 (2023) 114554, https://doi.org/10.1016/j.optmat.2023.114554.

[75] M. Jayachandiran, P. Balakrishnan, S.M.M. Kennedy, M.D. Bharathi, J. Nandhagopal, Comparative photoluminescence studies on the various trivalent rare-earth ions (Eu^{3+}, Dy^{3+}, Sm^{3+}, and Pr^{3+}) activated single-host material for solid-state lighting applications, J. Mater. Sci. Mater. Electron. 34 (2023) 106, https://doi.org/10.1007/s10854-022-09580-0.

[76] A. Layek, S. Banerjee, B. Manna, A. Chowdhury, Synthesis of rare-earth doped ZnO nanorods and their defect–dopant correlated enhanced visible-orange luminescence, RSC Adv. 6 (2016) 35892–35900, https://doi.org/10.1039/C6RA02278B.

[77] P. Halappa, A. Mathur, M.-H. Delville, C. Shivakumara, Alkali metal ion co-doped Eu^{3+} activated $GdPO_4$ phosphors: structure and photoluminescence properties, J. Alloys Compd. 740 (2018) 1086–1098, https://doi.org/10.1016/j.jallcom.2018.01.087.

[78] A.H. Qaisi, U.H. Kaynar, M. Ayvacikli, J. Garcia-Guinea, Y. Alajlani, M. Topaksu, N. Can, Novel Dy incorporated $Ca_3Y_2B_4O_{12}$ phosphor: insights into the structure, broadband emission, photoluminescence and cathodoluminescence characteristics, Appl. Radiat. Isot. 185 (2022) 110257, https://doi.org/10.1016/j.apradiso.2022.110257.

[79] G. Blasse, Energy transfer in oxidic phosphors, Phys. Lett. 28 (1968) 444–445, https://doi.org/10.1016/0375-9601(68)90486-6.

[80] D.A. Jabali, A.Y. Madkhli, G. Souadi, Ü.H. Kaynar, M.B. Coban, O. Madkhali, M. Ayvacikli, N. Amri, N. Can, Temperature-responsive insights: investigating Eu^{3+} and Dy^{3+} activated yttrium calcium oxyborate phosphors for structure and luminescence, Appl. Radiat. Isot. 206 (2024) 111214, https://doi.org/10.1016/j.apradiso.2024.111214.

[81] K. R, P. A, M.M. Kennedy S, V. Mishra, M.I. Sayyed, M. Rashad, S.D. Kamath, Evaluation of luminescent and thermal properties of Dy^{3+} doped tungstate phosphors for optoelectronic and thermometry applications, Phys. B Condens. Matter 697 (2025) 416712, https://doi.org/10.1016/j.physb.2024.416712.

[82] Y. Alajlani, N. Can, Novel Dy and Sm activated $BaSi_2O_5$ phosphors: insights into the structure, intrinsic and extrinsic luminescence, and influence of doping concentration, J. Lumin. 230 (2021) 117718, https://doi.org/10.1016/j.jlumin.2020.117718.

[83] J. Hong, Y. Liu, Y. Xu, X. Meng, H. Fan, J. Li, Z. Lin, Luminescence properties and energy transfer study of color temperature tunable $CaSrSiO_4$:Dy^{3+},Eu^{3+} white phosphors, Opt. Mater. 149 (2024) 115033, https://doi.org/10.1016/j.optmat.2024.115033.

[84] M. Deepali, Jayasimhadri, thermally stable and color-tunable bi-activated (Dy^{3+}/Eu^{3+}) alkaline Earth metasilicate phosphor for luminescent devices, RSC Adv. 13 (2023) 21105–21117, https://doi.org/10.1039/D3RA03229A.

[85] R.V. Yadav, R.S. Yadav, A.K. Singh, A. Bahadur, T.P. Yadav, S.B. Rai, Alkali ions effect on optical properties of Tm^{3+}, Yb^{3+} co-doped gadolinium tungstate phosphor, Mater. Chem. Phys. 215 (2018) 277–284, https://doi.org/10.1016/j.matchemphys.2018.05.008.

[86] R.S. Yadav, Monika, S.B. Rai, S.J. Dhoble, Recent advances on morphological changes in chemically engineered rare Earth doped phosphor materials, Prog. Solid State Chem. 57 (2020) 100267, https://doi.org/10.1016/j.progsolidstchem.2019.100267.

[87] P. Singh, R.S. Yadav, S.B. Rai, Enhanced photoluminescence in a Eu^{3+} doped $CaTiO_3$ perovskite phosphor via incorporation of alkali ions for white LEDs, J. Phys. Chem. Solid. 151 (2021) 109916, https://doi.org/10.1016/j.jpcs.2020.109916.

[88] S. Ponkumar, D. Prakashbabu, K. Parasuraman, R. Uthrakumar, K. Kaviyarasu, Synthesis, characterization, and enhanced photoluminescence of ZrO_2:Dy^{3+} phosphors by incorporating Li^+, Na^+ and K^+ ions for LED applications, Ceram. Int. 50 (2024) 13219–13228, https://doi.org/10.1016/j.ceramint.2024.01.233.

[89] Y. Zhai, L. Jiang, Y. Han, W. Wang, X. Chen, H. Wu, Microwave synthesis and luminescence properties of PO43− and alkali metal ions-doped $CaMoO_4$:Dy^{3+} phosphors, Optik 225 (2021) 165810, https://doi.org/10.1016/j.ijleo.2020.165810.

[90] A. Ozdemir, V. Altunal, Z. Yegingil, Effects of Na^+ cation on the luminescence enhancement and TL dosimetric properties of SrB_6O_{10}:Dy^{3+}, J. Alloys Compd. 1015 (2025) 178823 https://doi.org/10.1016/j.jallcom.2025.178823.

[91] V. Onar, E. Ekdal Karali, A.S. Altowyan, H. Aydin, U.H. Kaynar, C. Gök, M. B. Coban, J. Hakami, Y. Ozcan, A. Canimoglu, N. Can, Luminescence enhancement and thermal stability of alkali co-doped Eu^{3+}:$LaMgB_5O_{10}$ phosphors, Appl. Radiat. Isot. 226 (2025) 112219, https://doi.org/10.1016/j.apradiso.2025.112219.

[92] M. Monika, R.S. Yadav, A. Bahadur, S.B. Rai, Concentration and pump power-mediated color tunability, optical heating and temperature sensing via TCLs of red emission in an Er^{3+}/Yb^{3+}/Li^+ co-doped $ZnGa_2O_4$ phosphor, RSC Adv. 9 (2019) 40092–40108, https://doi.org/10.1039/C9RA09120C.

[93] R.S. Yadav Monika, A. Rai, S.B. Rai, NIR light guided enhanced photoluminescence and temperature sensing in Ho^{3+}/Yb^{3+}/Bi^{3+} co-doped $ZnGa_2O_4$ phosphor, Sci. Rep. 11 (2021) 4148, https://doi.org/10.1038/s41598-021-83644-9.

[94] R.S. Yadav, S.J. Dhoble, S.B. Rai, Enhanced photoluminescence in Tm^{3+}, Yb^{3+}, Mg^{2+} tri-doped $ZnWO_4$ phosphor: three photon upconversion, laser induced optical heating and temperature sensing, Sensor. Actuator. B Chem. 273 (2018) 1425–1434, https://doi.org/10.1016/j.snb.2018.07.049.

[95] J. Hakami, U.H. Kaynar, M.B. Coban, H. Aydin, R. Alamri, D.A. Jabali, N. Can, Optical performance and luminescence properties of Dy^{3+}-doped $LaMgB_5O_{10}$ phosphors, Inorg. Chem. Commun. 171 (2025) 113540, https://doi.org/10.1016/j.inoche.2024.113540.

[96] C. Liu, Y. Zheng, Y. Qin, L. Liang, S. Yang, H. Li, H. Jiang, X. Zhao, S. Liu, H. Zhang, J. Zhu, Study on a highly thermostable Dy^{3+}-Activated borophosphate phosphor, Inorg. Chem. 63 (2024) 6483–6492, https://doi.org/10.1021/acs.inorgchem.4c00358.

[97] L. Xiong, R. Cong, T. Yang, Bi^{3+}-sensitized Dy^{3+} emission for tunable luminescence and efficiency enhancement in $LiY_6O_5(BO_3)_3$ phosphors, Dalton Trans. 54 (2025) 12933–12943, https://doi.org/10.1039/D5DT01634G.

[98] P.A. Tejas, S. Masilla Moses Kennedy, K. Panda, M.I. Sayyed, T.A. Hanafy, S. D. Kamath, A comprehensive Study of nuanced properties of Dy^{3+}-Doped alkaline Earth silicates for noncontact thermometry applications, Luminescence 40 (2025), https://doi.org/10.1002/bio.70167.

[99] B. Baby, S. Thomas, J. Jose, K. Thomas, P. Punathil, N.V. Unnikrishnan, P.R. Biju, C. Joseph, Luminescence studies and Judd Ofelt parameterization of Dy^{3+} activated $La_2(WO_4)_3$ yellow phosphor, Inorg. Chem. Commun. 165 (2024) 112550, https://doi.org/10.1016/j.inoche.2024.112550.

[100] A.U. Ahmad, S. Hashim, S.K. Ghoshal, Spectroscopic characteristics of Dy^{3+} impurities–doped borate-based glasses: Judd–Ofelt calculation, Mater. Chem. Phys. 253 (2020) 123386, https://doi.org/10.1016/j.matchemphys.2020.123386.

[101] M. İlhan, İ.Ç. Keskin, L.F. Güleryüz, M.İ. Katı, A comparison of spectroscopic properties of Dy^{3+}-doped tetragonal tungsten bronze MTa_2O_6 (M = Sr, Ba, Pb) phosphors based on Judd–Ofelt parameters, J. Mater. Sci. Mater. Electron. 33 (2022) 16606–16620, https://doi.org/10.1007/s10854-022-08557-3.

[102] M. İlhan, İ.Ç. Keskin, Analysis of Judd–Ofelt parameters and radioluminescence results of $SrNb_2O_6$:Dy^{3+} phosphors synthesized via molten salt method, Phys. Chem. Chem. Phys. 22 (2020) 19769–19778, https://doi.org/10.1039/D0CP02256J.

[103] M. Qu, X. Zhang, X. Mi, H. Sun, Q. Liu, Z. Bai, Novel and wide-ranging color tuning photoluminescence properties of Tb^{3+}/Eu^{3+} doped garnet-type $Li_3Lu_3Te_2O_{12}$ phosphor: energy transfer and enhanced thermal stability, J. Alloys Compd. 872 (2021) 159506, https://doi.org/10.1016/j.jallcom.2021.159506.

[104] Y. Ling, R. Cui, X. Guo, P. Linghu, R. Zhao, C. Deng, Thermally-stable and color-tunable novel single phase phosphor Ca_2GaTaO_6:Dy^{3+}, Sm^{3+} for indoor lighting applications, Ceram. Int. 50 (2024) 14188–14199, https://doi.org/10.1016/j.ceramint.2024.01.325.

[105] S.W. Awaghade, G.B. Nair, N.S. Dhoble, S.J. Dhoble, White light emitting $Sr_3YNa(PO_4)_3F$: Dy^{3+}, Eu^{3+} fluorapatite phosphor with tunable correlated color temperature, J. Opt. (2025), https://doi.org/10.1007/s12596-025-02710-x.